



# Synergetic effect of the interface electric field and the plasmon electromagnetic field in Au-Ag alloy mediated Z-type heterostructure for photocatalytic hydrogen production and CO<sub>2</sub> reduction

Qi Li<sup>a</sup>, Shengchao Yang<sup>a,\*</sup>, Ruihan Liu<sup>a</sup>, Yufan Huang<sup>a</sup>, Yuwei Liang<sup>a</sup>, Chunling Hu<sup>a</sup>,  
Min Wang<sup>b</sup>, Zhiyong Liu<sup>a,\*</sup>, Yanlong Tai<sup>a,c</sup>, Jichang Liu<sup>a,d</sup>, Yongsheng Li<sup>a,d,\*\*</sup>

<sup>a</sup> School of Chemistry and Chemical Engineering, Shihezi University/Key Laboratory of Green Process for Chemical Engineering/Key Laboratory for Chemical Materials of Xinjiang Uygur Autonomous Region/Engineering Center for Chemical Materials of Xinjiang Bingtuan, Shihezi University, Xinjiang, Shihezi 832003, China

<sup>b</sup> Key Lab of High Performance Ceramics and Superfine Microstructure, Shanghai Institute of Ceramics, Chinese Academy of Sciences, 1295 Ding-xi Road, Shanghai 200050, China

<sup>c</sup> Key Laboratory of Human-Machine Intelligence-Synergy Systems of Chinese Academy of Sciences (CAS), Shenzhen Institutes of Advanced Technology, CAS, Shenzhen 518055, China

<sup>d</sup> Lab of Low-Dimensional Materials Chemistry Key Laboratory for Ultrafine Materials of Ministry of Education School of Materials Science and Engineering, East China University of Science and Technology, Shanghai 200237, China

## ARTICLE INFO

### Keywords:

Photocatalysis  
Localized surface plasmon resonance  
Heterostructure  
Dual electric field  
Au-Ag alloy

## ABSTRACT

The challenge of synergistically optimizing different mechanisms limits the further improvement of plasmon-mediated photocatalytic activities. In this work, the CdS/Au-Ag/B-TiO<sub>2</sub> photocatalyst, combining a hetero-junction structure with localized surface plasmon resonance (LSPR), is prepared by a high-temperature hydrogen reduction and hot solvent method. The novel synergistic interaction at the interface between the electric field and the plasmon electromagnetic field drives effective charge separation with improved photocatalytic efficiency. The Cd3Ti2 catalyst exhibits the highest photocatalytic activity, and the H<sub>2</sub> generation efficiency under the full solar spectrum is 15.97 mmol·h<sup>-1</sup>·g<sup>-1</sup> with good stability as high as 81.3% in 24 h cycles. The CH<sub>4</sub> and CO precipitation performances are achieved at 14.2 μmol·h<sup>-1</sup>·g<sup>-1</sup> and 113.9 μmol·h<sup>-1</sup>·g<sup>-1</sup>, respectively, in the CO<sub>2</sub>RR process. The design of the synergistic mechanism of the dual electric field offers an important development in the field of plasma-mediated photoredox catalysis.

## 1. Introduction

Effective solar energy harvesting and conversion is a potential solution to the energy crisis [1]. Among various technologies, plasmonic photocatalysts have received significant attention, and research on localized surface plasmon resonance (LSPR) has achieved unprecedented development for enhancing light absorption in a wide spectral range. In plasma-mediated systems, the effects of the LSPR excitation from metal nanostructures supported on the semiconductor are divided into three types, including plasmon-induced direct electron transfer (DET) [2], local electromagnetic field enhancement (LEMF), and plasmon-induced resonance energy transfer (RET) [3,4]. Although some

mechanisms of plasmon-mediated photoredox catalysis have been recognized, it is still a challenge to develop the synergy effects between different mechanisms to achieve the organic integration of multiple functions.

Au and Ag appear in many studies as co-catalysts or plasma components. Ag or Au nanoparticles have been used for high-efficiency photocatalytic hydrogen production as a co-catalyst. Yu et al. rationally designed a core-shell TiO<sub>2</sub>/Au@NiS<sub>1+x</sub> structure with an H<sub>2</sub> production rate of 9616 μmol·h<sup>-1</sup>·g<sup>-1</sup> and an apparent quantum efficiency of 46% at 365 nm [5]. Wang et al. reported a novel Z-scheme system based on the Au decorated 5,10,15,20-tetrakis (4-trimethylammonio-phenyl) porphyrin tetra (p-toluene sulfonate) functionalized iron-doped

\* Corresponding authors.

\*\* Corresponding author at: School of Chemistry and Chemical Engineering, Shihezi University/Key Laboratory of Green Process for Chemical Engineering/Key Laboratory for Chemical Materials of Xinjiang Uygur Autonomous Region/Engineering Center for Chemical Materials of Xinjiang Bingtuan, Shihezi University, Xinjiang, Shihezi 832003, China.

E-mail addresses: [shengchao.yang@shzu.edu.cn](mailto:shengchao.yang@shzu.edu.cn) (S. Yang), [lzyongclin@sina.com](mailto:lzyongclin@sina.com) (Z. Liu), [ysli@ecust.edu.cn](mailto:ysli@ecust.edu.cn) (Y. Li).

<https://doi.org/10.1016/j.apcatb.2023.122700>

Received 20 December 2022; Received in revised form 7 March 2023; Accepted 25 March 2023

Available online 27 March 2023

0926-3373/© 2023 Elsevier B.V. All rights reserved.

carbon nitride. The  $\text{H}_2$  evolution activity of  $3172.2 \mu\text{mol}\cdot\text{h}^{-1}\cdot\text{g}^{-1}$  under UV-Vis irradiation was achieved by promoting the surface redox activities via efficient charge separation and transfer [6]. Meanwhile, amorphous  $\text{AgSe}_x$  was incorporated in situ onto metallic Ag as a novel and excellent  $\text{H}_2$ -evolution active site to boost the interfacial  $\text{H}_2$ -generation of Ag nanoparticles in a  $\text{TiO}_2/\text{Ag}$  system. The as-prepared  $\text{TiO}_2/\text{Ag}@\text{AgSe}_x$  photocatalyst exhibited the  $\text{H}_2$ -production rate of  $853 \mu\text{mol}\cdot\text{h}^{-1}\cdot\text{g}^{-1}$  [7]. During the LSPR excitation, some hot electrons in plasma may gain enough energy to inject into the conduction band of the adjacent semiconductor. Such a process is called plasmon-induced DET [8]. Franco et al. have experimentally unraveled the ultrafast photo-physics of CdSe nanorods (NRs) and CdSe-Au HNPs, using a 2DES to describe the two-step relaxation of hot carriers [9]. In the work of Chen et al., the Au/ $\text{XS}_2$  core@shell nanostructures with well-controlled multilayers of the shell [10]. The unique Au/ $\text{XS}_2$ /Au antenna-reactor hybrids were synthesized using a hydrothermal method for the first time, which enhanced the transfer of hot electrons with improved photocatalytic hydrogen production performance up to  $51.6 \mu\text{mol}\cdot\text{g}^{-1}\cdot\text{h}^{-1}$ . Li et al. realized that plasma hot electrons from oxygen vacancies could be used for the infrared-driven catalytic  $\text{CO}_2$  reduction on  $\text{Bi}_2\text{O}_{3-x}$ , which enabled the efficient photocatalysis of  $\text{CO}_2$  to CO ( $\sim 100\%$  selectivity,  $16.15 \mu\text{mol}\cdot\text{g}^{-1}\cdot\text{h}^{-1}$ ) [11]. Dhiman et al. showed the tuning of the catalytic behavior of dendritic plasmonic colloidosomes (DPCs) in plasmonic hotspots, which successfully converted  $\text{CO}_2$  to methane ( $1.5 \mu\text{mol}\cdot\text{g}^{-1}\cdot\text{h}^{-1}$ ) at atmospheric pressure and room temperature, driven by sunlight [12]. Li's research team used  $\text{H}_2\text{O}$  as an electron donor to achieve unassisted and highly selective gas phase  $\text{CO}_2$  reduction on a plasma-driven Au/p-GaN photocatalyst using photo-excited hot carriers. Its CO precipitation performance reached  $650 \mu\text{mol}\cdot\text{g}^{-1}\cdot\text{h}^{-1}$  [13]. Sistani et al. researched plasma-driven hot electron transfer at atomic-sharp metal-semiconductor nanojunctions, and the ability of momentum matching was demonstrated by controlling the energy distribution of the injected plasmon-driven hot electron [14].

Apart from the DET effect, the LEMF and RET effects are also important. LEMF can significantly boost the interband transition rate in the adjacent semiconductor if the plasmon resonance energy is larger than the semiconductor bandgap. On the other hand, the plasmonic oscillation energy could be transferred in the RET to the semiconductor photocatalysts through the EM field or non-radiative dipole-dipole coupling, which requires spectral overlap between the metal LSPR band and the light absorption range of the semiconductor [8,15,16]. The surface plasmon may improve the electron-hole pair generation and separation by these two mechanisms. Ma et al. prepared a core-shell (Au/AgAu)@CdS hybrid nanostructure with strong multi-interfacial plasmon coupling. The strong plasmon absorption and near-field enhancement can boost the generation and separation of electron-hole pairs in the multigap photocatalysts [17]. Yang et al. developed a dual-plasmonic-antenna strategy that efficiently generates energetic hot electrons with strong electromagnetic fields to boost photocatalytic hydrogen evolution ( $191.2 \text{ mmol}\cdot\text{g}^{-1}\cdot\text{h}^{-1}$ ) [18]. Wang et al. used an asymmetric synthetic method to prepare Au-CdSe core-semi-shell nanorods for plasmon near-field-enhanced visible-light-driven hydrogen evolution (with a yield of  $262.3 \mu\text{mol}\cdot\text{g}^{-1}\cdot\text{h}^{-1}$ ) [19]. Wang et al. have developed a facile surfactant-free nanofabrication approach to embed Au nanoparticles in N-doped  $\text{TiO}_2$  nanobowl arrays. The utilization of plasmonics in charge generation and separation by RET was well synergized with the Schottky junctions for enhanced photocatalytic water splitting, achieving the  $\text{H}_2$  production rates of  $637 \mu\text{mol}\cdot\text{g}^{-1}\cdot\text{h}^{-1}$  illuminated with the full solar spectrum and  $132 \mu\text{mol}\cdot\text{g}^{-1}\cdot\text{h}^{-1}$  with visible light only [20]. Gao et al. revealed the polarization effect in surface plasmon-Induced photocatalysis on Au/ $\text{TiO}_2$  nanoparticles [21]. Vahidzadeh et al. reported that the highest electric field intensities were found between the Ag- $\text{TiO}_2$  and Ag-air interfaces. Under AM1.5 illumination, the highest rate of  $\text{CH}_4$  production of  $9.38 \mu\text{mol}\cdot\text{g}^{-1}\cdot\text{h}^{-1}$  was achieved on the AgCu-TNTA [22].

LSPR is a promising strategy for improving solar energy conversion

in plasmonic-enhanced photocatalysis. However, achieving efficient charge transfer with effective charge separation in metal/semiconductor systems is still challenging. In some cases, the near-field of isolated plasmonic nanoparticles cannot efficiently promote the charge dynamics in adjacent semiconductor photocatalysts. One possible way to solve this issue is the combination of two different types of metal nanoparticles in the same nanostructure to establish bimetallic nanoparticles (BNPs) [23,24]. Compared with isolated single metal nanoparticles (MNP), BNPs exhibit a much stronger local plasmonic effect with a highly strengthened EM field due to their synergetic effect of its constituent elements at the metal-semiconductor interface. It has been reported that the electromagnetic field intensity of localized "hot spots" can reach 1000-fold of the far-field excitation light, electromagnetic field intensity based on the finite-difference time-domain (FDTD) simulations with discrete dipole approximation (DDA) methods [8,21,25]. Among many metals with LSPR effect, Ag offers excellent performance. However, its chemical stability limits its application. Au has better stability than Ag, but its LSPR strength is weak. Au-Ag alloys often show better enhanced catalytic activity than the isolated Au or Ag particles due to the stronger LSPR and higher stability under photoexcitation [26, 27]. Au-Ag alloy-mediated Z-type heterostructure can accelerate electron migration with improved electron-hole separation due to the synergetic effect of the electric field at the interface. The plasmonic electromagnetic field helps to reduce the random migration of low-energy photoexcited electrons and holes in the electronic medium and drives high-energy electrons to participate in the photocatalytic reactions, such as carbon dioxide reduction or hydrogen production.

In this work, we propose combining the LSPR with a heterogeneous electronic structure to achieve efficient charge transfer and separation. It is based on constructing the synergistic dual electric fields between the interfacial electric field and the plasmon electromagnetic field, which improves the vector charge transfer kinetics, resulting in a much improved photocatalytic carbon dioxide reduction performance with an optimal  $\text{CH}_4$  production rate of  $14.2 \mu\text{mol}\cdot\text{g}^{-1}\cdot\text{h}^{-1}$  and HER performance for an  $\text{H}_2$  production rate of  $15.97 \text{ mmol}\cdot\text{g}^{-1}\cdot\text{h}^{-1}$ . First, we synthesized the  $\text{TiO}_2(\text{B})$  with a standard hydrothermal method, which was reduced in an  $\text{H}_2$  environment at high temperature to B- $\text{TiO}_2$  with a broadened light absorption wavelength range from visible to near-infrared. Au-Ag nanoparticles were synthesized separately in a standard method, which was impregnated onto the reduced B- $\text{TiO}_2$  to form Au-Ag/B- $\text{TiO}_2$  composite photocatalysts with different concentrations of Au-Ag. While, Since the plasmonic bands of Au-Ag alloys nanoparticles are mainly located in the visible wavelength range, the coupling between Au-Ag and B- $\text{TiO}_2$  can effectively improve solar energy utilization through the RET mechanism. Hence, light absorption is no longer limited by the semiconductor bandgap energy. The finite-difference time domain (FDTD) methods represent a reasonable foundation for the LEMF mechanism. Since the three plasma energy transfer mechanisms are not mutually exclusive, it is expected that the RET mechanism and the LEMF mechanism will play major roles in the performance enhancement of the catalytic system [28,29]. In addition, when constructing the  $\text{Au}_3\text{Ag}_7\text{-TiO}_2$  and  $\text{Au}_3\text{Ag}_7\text{-CdS}$  dielectric surrounding, the interfacial electric field can directly improve the vector charge transfer process, driving photoelectrons transfer from the semiconductors to the metallic NPs, which is verified by the DFT calculations. The band energy levels of CdS match well with those of  $\text{TiO}_2$ . The existence of the dual-phase of  $\text{TiO}_2$  (anatase/ $\text{TiO}_2(\text{B})$ ) also enables the CdS/Au-Ag/anatase/ $\text{TiO}_2(\text{B})$  system to form both II-type and Z-type composite heterojunctions. Effective charge separation will allow more electrons to participate in photocatalytic redox reactions [30]. The collaboration between the electric field at the interface and the plasma electromagnetic field offers the possibility of a fully optimized photocatalyst with an extended wavelength of light absorption and improved charge separation, which will become an important field in plasma-mediated photoredox catalysis.

## 2. Experimental section

### 2.1. Materials

Ethylene glycol ((CH<sub>2</sub>OH)<sub>2</sub>), titanium tetrachloride (TiCl<sub>4</sub>), silver nitrate (AgNO<sub>3</sub>), sodium borohydride (NaBH<sub>4</sub>), trisodium citrate dihydrate (C<sub>6</sub>H<sub>5</sub>Na<sub>3</sub>O<sub>7</sub>), chloroauric acid (HAuCl<sub>4</sub>·4 H<sub>2</sub>O), cadmium nitrate (Cd(NO<sub>3</sub>)<sub>2</sub>·6 H<sub>2</sub>O) and thiourea (CH<sub>4</sub>N<sub>2</sub>S) were purchased from Shanghai Aladdin Biochemical Technology Co., Ltd. Ethylenediamine (C<sub>2</sub>H<sub>8</sub>N<sub>2</sub>) is supplied by Tianjin Shengao Chemical Reagent Co., Ltd. All chemicals are analytical grade, and used without further purification.

### 2.2. Synthesis of TiO<sub>2</sub>(B) and B-TiO<sub>2</sub>

First, based on our previous work [31], 60 mL ethylene glycol was added to an 80 mL PTFE-lined stainless steel hydrothermal reactor. Then, 1 mL TiCl<sub>4</sub> was added to the suspension until no HCl gas was formed at room temperature. After that, 1 mL of deionized water was added to the mixture. The sealed autoclave was heated in an oven at 150 °C for 4 h. Finally, the TiO<sub>2</sub>(B) nanoflower product was collected by centrifuge. The impurities were removed by washing the solid with distilled water and absolute ethanol. The cleaned sample was vacuumed and dried for 24 h at 60 °C. The sample TiO<sub>2</sub>(B) was calcined at 350 °C, 450 °C, and 550 °C in H<sub>2</sub>/Ar (5%/95%) atmosphere to obtain mixed phase B-TiO<sub>2</sub> with different components (350-HB, 450-HB, and 550-HB). The prepared TiO<sub>2</sub>(B) was added to a corundum crucible and heated in a muffle furnace at 550 °C with a heating rate of 5 °C/min for 2 h before the anatase sample was collected (550-AirB).

### 2.3. Synthesis of Au-Ag/B-TiO<sub>2</sub>

Au-Ag alloy NPs were deposited on the B-TiO<sub>2</sub> by an impregnation method. The detailed method for producing Au-Ag alloy is shown in the [supplementary materials](#). For impregnation, 10 mL Au-Ag NP dispersion was added to a tube containing 50 mg B-TiO<sub>2</sub>. The dispersion solution was thoroughly mixed using an ultrasonic disperser and then placed in a drying oven at 60 °C. The dried sample was collected and stored in the dark.

### 2.4. Synthesis of CdS/Au-Ag/B-TiO<sub>2</sub>

Five CdS/Au-Ag/B-TiO<sub>2</sub> samples (Cd1Ti4, Cd2Ti3, Cd1Ti1, Cd3Ti2, and Cd4Ti1) were synthesized with different weight ratios of 1:4, 2:3, 1:1, 3:2, and 4:1 between CdS and Au-Ag/B-TiO<sub>2</sub>. Cd(NO<sub>3</sub>)<sub>2</sub>·6 H<sub>2</sub>O (0.966, 1.287, 1.159, 1.159, and 1.545 g) was mixed with the corresponding Au-Ag/B-TiO<sub>2</sub> (1, 0.5, 0.3, 0.2, and 0.1 g) precursor and CH<sub>4</sub>N<sub>2</sub>S (0.711, 0.949, 0.854, 0.854, and 1.138 g) in 30 mL ethylenediamine respectively. The solution was transferred to a 100 mL PTFE-lined autoclave and heated at 180 °C for 24 h. After the reaction, the sample was cooled to room temperature before being washed with ethanol and distilled water several times. The samples were vacuum-dried at 60 °C overnight. Pure CdS nanowires were synthesized following the same hydrothermal conditions without adding Au-Ag/B-TiO<sub>2</sub>.

### 2.5. Characterization

Bruker D8 ADVANCE A25X X-ray diffractometer (AXS Co., Ltd.) was used to analyze the crystal structures of the samples. BET specific surface areas were measured with a QDS-MP-30 surface area analyzer. The microstructures were observed on a scanning electron microscope (SEM, Inspect F50, FEI) and a transmission electron microscope (TEM, JEM-2100 F, JEOL). The ultraviolet-visible (UV-Vis) diffuse reflectance spectra (UV-vis-DRS) were collected on a UV-Vis spectrophotometer (UV-2600, Shimadzu). X-ray photoelectron spectroscopy (XPS, ESCALA 250, Thermal Fisher) was used to analyze the elemental composition

and oxidation status. All binding energies were calibrated using the C 1 s peak at 284.8 eV. The photoluminescence (PL) spectrum was measured with a fluorescence spectrophotometer (LS55, Perkin Elmer) under the excitation wavelength of 315 nm. Electron paramagnetic resonance (EPR) spectra were measured at 77 K with an electron paramagnetic resonance spectrometer (JES-FA200, JEOL). Photoelectrochemical (PEC) measurements were performed on an electrochemical workstation (CHI 660E, Shanghai Chenhua Instrument Company). The photocatalytic reaction performances (HER and CO<sub>2</sub>RR) were evaluated on a closed Pyrex gas circulation system (LabSolar 6 A, Beijing Perfectlight Co., Ltd.) at the atmospheric pressure with an irradiation cell at the top with the details in the [supplementary materials](#).

### 2.6. FDTD simulations

The three-dimensional FDTD method was used to simulate the near-field distributions of the coupled nanoparticles. CdS/Au-Ag/TiO<sub>2</sub> materials were illuminated by a plane wave in the simulation with an excitation wavelength of 520 nm. Dielectric properties of different materials were obtained from the DFT calculations. The initial sizes and shapes of Au-Ag alloy, CdS, and TiO<sub>2</sub> in the simulation were estimated from the SEM and TEM images, as shown in [Fig. 9](#). The Au-Ag alloy hollow nanospheres have a radius of 20 nm and a shell thickness of 10 nm. The CdS nanowire has a diameter of about 40 nm, simulated by a cylinder with a radius of 20 nm and a length of 70 nm. Due to the irregular morphology of TiO<sub>2</sub>, a bulk crystal model was used in the modeling. For easier comparison of electromagnetic strength, its modeling is consistent with CdS.

### 2.7. DFT calculations

First-principles calculations were carried out to investigate the properties of CdS/Au<sub>3</sub>Ag<sub>7</sub>/TiO<sub>2</sub> using the Vienna Ab-initio Simulation Package (VASP) [32]. The interaction between ions and valence electron densities is described using the projector augmented wave (PAW) potentials, and GGA-PBE is selected to treat the exchange correlation [33]. The cutoff energy of 450 eV was used for all calculations. The k-point mesh of 2 × 2 × 1 was used. The relaxation of the electronic degrees of freedom is assumed to be converged when the total energy changes between the two electronic optimization steps are smaller than 1 × 10<sup>-5</sup> eV, and the force below 0.05 eV/Å for ions was used as the criterion for relaxation convergence. The van der Waals effects were also considered with Grimme's DFT-D3 method [34,35].

## 3. Results and discussion

### 3.1. Structure characterization of the photocatalysts

The crystal structure, composition, and crystalline phases of the synthesized samples were characterized by X-ray diffraction (XRD). The XRD patterns of the pure TiO<sub>2</sub>(B) and B-TiO<sub>2</sub> are shown in [Fig. 1\(a\)](#). The pure TiO<sub>2</sub>(B) diffraction peaks can be indexed to the monoclinic titanium dioxide (JCPDS no. 46-1238). After high-temperature hydrogen reduction, the 350-HB, 450-HB, and 550-HB samples show the three major peaks at 25.3°, 37.8°, and 48°, which are assigned to the (101), (004), and (200) crystal planes of the anatase phase (JCPDS no. 21-1272) [36]. The diffraction peak intensity of the anatase phase increases gradually with the increase in temperature, which indicates that crystallinity was improved as the reduction temperature was increased [37]. Therefore, the sample reduced at 550 °C (550-HB) was selected as the substrate for the subsequent deposition of Au-Ag and CdS. Interestingly, at the same temperature of 550 °C, the XRD pattern of 550-HB is different from that of the sample annealed in the air (550-AirB). The peaks of (103), (112), (105), and (211) were not observed in the 550-HB. Meanwhile, the peaks in 550-HB have larger widths than 550-AirB, demonstrating some amorphous structure was formed in the 550-HB

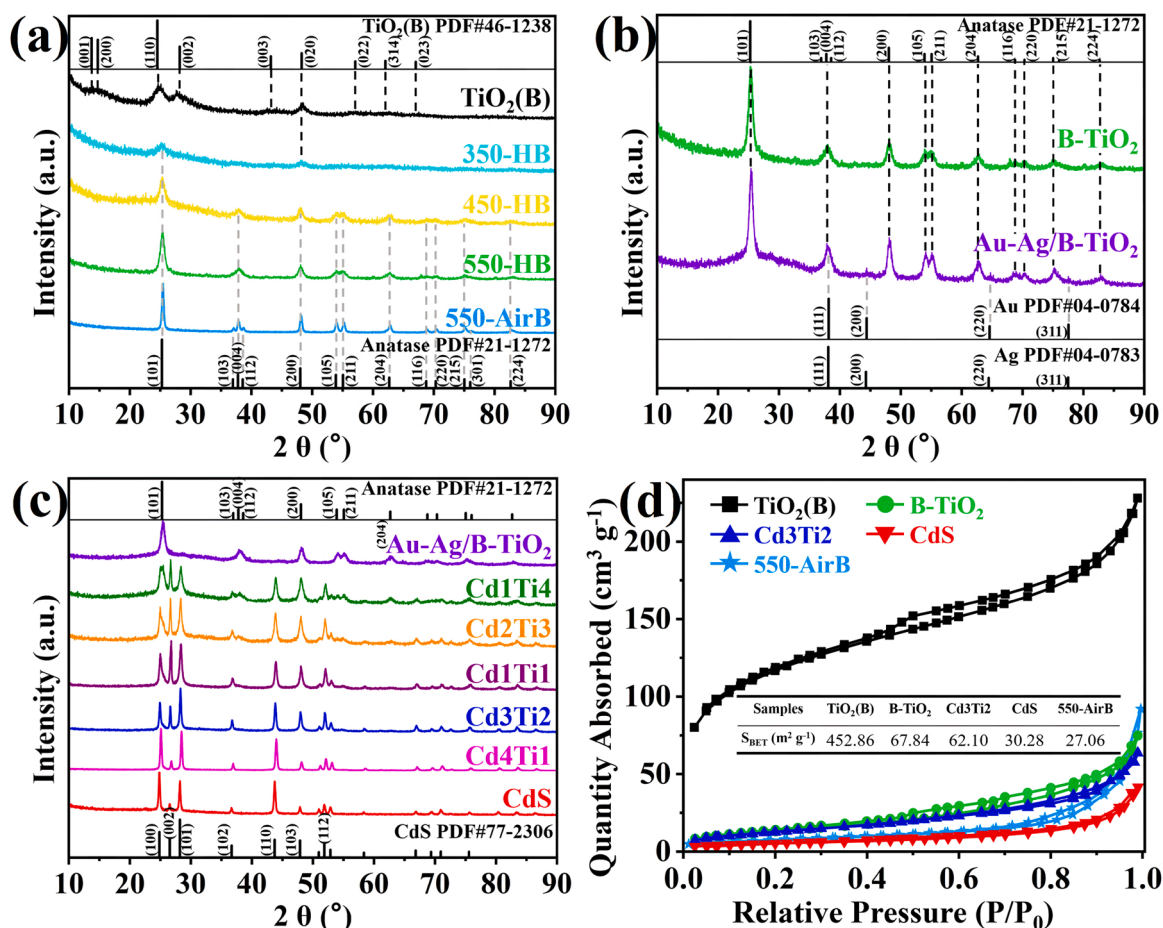


**Fig. 1.** XRD patterns of (a) the pure TiO<sub>2</sub>(B) and B-TiO<sub>2</sub> after high-temperature hydrogen reduction, (b) Au-Ag/B-TiO<sub>2</sub>, and (c) the pure CdS and the composite samples. (d) N<sub>2</sub> adsorption-desorption isotherms for TiO<sub>2</sub>(B), B-TiO<sub>2</sub>, CdS, Cd3Ti2, and 550-AirB.

[38]. To further determine the phase structure of 550-HB, we compared the XRD patterns of pure TiO<sub>2</sub>(B) and 550-HB using finer crystallographic information as a reference. What can be seen is that the (001), (200), (201), (310), (402), (003), (610), (712), (621), and (024) crystal planes belonging to TiO<sub>2</sub>(B) can all be observed from the 550-HB (Fig. S1). Hence, the 550-HB has a mixed anatase phase and TiO<sub>2</sub>(B), with anatase being the main component [36,39].

Fig. 1(b) shows the XRD pattern of the Au-Ag/B-TiO<sub>2</sub>. The diffraction peaks of the B-TiO<sub>2</sub> remained unchanged before and after adding the Au-Ag alloy, indicating that the added Au-Ag alloy does not affect the crystal structure of the B-TiO<sub>2</sub>. The additional diffraction peaks at 38.1°, 44.3°, 64.4°, and 77.5° are indexed to the (111), (200), (220), (311) crystal planes of Au (JCPDS no. 04-0784) and Ag (JCPDS no. 04-0783) [40], respectively. Au and Ag have similar lattice constants. Therefore Au-Ag alloy has diffraction peaks similar to those of Au and Ag, consistent with previous reports [24]. In the Au-Ag/B-TiO<sub>2</sub> samples, Au and Ag diffraction peaks are very weak, owing to the good dispersion of lower content of Au-Ag. Nevertheless, the formation of Au-Ag alloy was identified in Fig. S3 [41]. The XRD spectra of the CdS/Au-Ag/B-TiO<sub>2</sub> composite samples with different CdS contents are shown in Fig. 1(c). The pure CdS shows the characteristic diffraction peaks at 24.8°, 26.5°, 28.2°, 43.7°, and 47.9°, attributed to the (100), (002), (101), (110), and (103) crystal planes, respectively, of the hexagonal wurtzite CdS (JCPDS no. 77-2306). Additional two weak peaks at 36.7° and 51.9° of the CdS crystals in the composite samples assigned to the (102) and (112) planes of the wurtzite CdS. Meanwhile, the characteristic peaks of B-TiO<sub>2</sub> were also observed distinctly in the CdS/Au-Ag/B-TiO<sub>2</sub> samples. With the increase of CdS loading, the intensities of the CdS peaks were progressively enhanced, while the relative intensities of the B-TiO<sub>2</sub> XRD signals

were decreased accordingly. The results indicate the coexistence of B-TiO<sub>2</sub> and CdS in the heterostructured composite [42].

The specific surface areas of the samples were investigated by BET gas-sorption measurements. Fig. 1(d) shows the N<sub>2</sub> adsorption-desorption isotherms for TiO<sub>2</sub>(B), B-TiO<sub>2</sub>, CdS, and Cd3Ti2. The Cd3Ti2 was selected as the comparison sample since it offered the best photocatalytic and electrochemical performance. The nitrogen adsorption-desorption isotherms of TiO<sub>2</sub>(B), B-TiO<sub>2</sub>, and Cd3Ti2 show the typical type IV curves with the TiO<sub>2</sub>(B) and B-TiO<sub>2</sub> showing the typical H3 hysteresis loops, meaning that the materials have slit holes formed by lamellae and particles, which was confirmed by the subsequent morphological studies (Fig. S3) [43]. The measured specific BET surface areas of the TiO<sub>2</sub>(B), B-TiO<sub>2</sub>, Cd3Ti2, and CdS were 452.86, 67.81, 62.1, and 23.63 m<sup>2</sup> g<sup>-1</sup>, respectively. The lower surface area of the B-TiO<sub>2</sub> compared to the TiO<sub>2</sub>(B) was attributed to the transformation of TiO<sub>2</sub>(B) nanosheets into TiO<sub>2</sub> nanoparticles during the high-temperature hydrogen reduction. The CdS shows a type II physorption isotherm curve. Because of this, the void structure of the sample Cd3Ti2, composed of B-TiO<sub>2</sub> and CdS, has the structural features of both components with less distinctive of the H3-type hysteresis loop. The capillary condensation brought by the slit pores is beneficial to the adsorption of reactants. A heterostructured photocatalyst with a large specific surface area offers a high density of active sites and facilitates photo-generated carrier transport for redox reactions, making it favorable for enhancing photocatalytic performance [42,44].

The morphology and microstructure of Au-Ag alloy, TiO<sub>2</sub>(B), B-TiO<sub>2</sub>, CdS, and CdS/Au-Ag/B-TiO<sub>2</sub> were studied by SEM and TEM. The SEM images of the Au-Ag alloy are shown in Fig. S3 (a-c), with an average particle size of ~40 nm. A film structure on the particle surface may be



due to the residual citrate ligand. TEM (Fig. 3(a) and (b), Fig. S2 (c) and (d)) images identified the hollow nanoparticulate structure of the Au-Ag alloy. Fig. S3 (d-f) shows the SEM images of the  $\text{TiO}_2(\text{B})$  with a spherical nanoflower morphology at a dimension of 200–500 nm formed by stacking nanosheets, consistent with previous reports. Hence, it is expected to have a high specific surface area, as confirmed by the BET results in Fig. 1(d). After high-temperature calcination in  $\text{H}_2$ , the nanosheet structure of  $\text{TiO}_2(\text{B})$  changed to fine particles with irregular spherical B- $\text{TiO}_2$  structure (200–500 nm) (Fig. S3 (g-i)), formed by the accumulation of small particles in the range of 20–50 nm. Meanwhile, Au-Ag alloy was successfully deposited on the B- $\text{TiO}_2$ , as shown in Fig. 2 (a-d), demonstrated by some small particles attached to the surface of B- $\text{TiO}_2$ , forming the Au-Ag/B- $\text{TiO}_2$  heterojunction [45]. Pure CdS shows a regular nanowire morphology with a relatively smooth surface. The average length is  $\sim 5 \mu\text{m}$  with a diameter of 40 nm, measured from the images in Fig. 2(e-g). Fig. 2(h-j) show the SEM images of the best-performing composite sample, Cd3Ti2. There is no obvious damage to the Au-Ag/B- $\text{TiO}_2$  structure in the solvothermal synthesis of CdS nanowires. Fig. S4 (a-f) show the SEM images of CdS/Au-Ag/B- $\text{TiO}_2$  samples with a different CdS content, which show the significant structural changes of the CdS nanowires due to the addition of Au-Ag/B- $\text{TiO}_2$ . It should be noted that with the increase of added Au-Ag/B- $\text{TiO}_2$ , the CdS nanowires become shorter. Hence, Au-Ag/B- $\text{TiO}_2$  could inhibit the growth of CdS nanowires along the axial direction [42,46].

The surface structure and morphology of Au-Ag alloy and Cd3Ti2 were further examined with TEM. Fig. 3(a) and (b) show that the Au-Ag alloy has a uniform hollow nanoparticulate structure with a size of 40–50 nm and a shell thickness of 20 nm. The lattice fringes of Au-Ag alloy give the lattice spacings of 0.235 and 0.204 nm observed in a high-resolution transmission electron microscope (HRTEM) could be

indexed to the (111) and (200) crystal planes of the Au-Ag alloy (Fig. 3 (c)). Besides, energy-dispersive X-ray spectroscopy (EDS) mapping analysis shows a homogeneous distributed Au and Ag in the Au-Ag alloy, which further confirms that the Au-Ag solid solution was successfully prepared at the Au: Ag atomic ratio of 3:7.

The TEM images in Fig. S5 reveal that the Au-Ag alloy nanoparticles were evenly dispersed on the  $\text{TiO}_2$  surface. To demonstrate that Au-Ag alloy nanoparticles have good interaction with the  $\text{TiO}_2$  surface, the structures of Au-Ag/ $\text{TiO}_2(\text{B})$  (Fig. S5 (a-c)) and Au-Ag/B- $\text{TiO}_2$  (Fig. S5 (d-f)) were investigated [47]. Au-Ag alloy nanoparticles were deposited via a dipping method. They are all contacting interfaces, and there exists an interaction between Au-Ag alloy and  $\text{TiO}_2$ . Here, we speculate that a certain amount of citrate ions were left on the surface of the Au-Ag alloy during the synthesis, which helps to interact with the oxygen vacancies (Ovs) or surface OH groups on the  $\text{TiO}_2(\text{B})$  and B- $\text{TiO}_2$  surfaces. The direct coupling of Au-Ag NPs and B- $\text{TiO}_2$  is conducive to transporting electrons between two materials [45]. Further observation of the lattice fringes of the Au-Ag/B- $\text{TiO}_2$  shows the lattice spacings of 0.240, 0.352, and 0.358 nm, corresponding to the (001), (101) planes of anatase and the (110) plane of  $\text{TiO}_2(\text{B})$ , respectively (Fig. 3(d)).

The TEM images further confirm the coupling of Au-Ag NPs, B- $\text{TiO}_2$ , and CdS in CdS/Au-Ag/B- $\text{TiO}_2$ . Fig. 3(i-j) show the CdS crystals in the sample Cd3Ti2 having a nanowire morphology. Au-Ag NPs, as the intermediate medium, are sandwiched between B- $\text{TiO}_2$  and CdS nanowires. The well-defined boundaries between the Au-Ag/B- $\text{TiO}_2$  and CdS nanowires indicate the successful formation of the heterojunctions in the composite (Fig. 3(k)). A magnified area of the CdS/Au-Ag/B- $\text{TiO}_2$  heterojunction is shown in Fig. 3(l). The catalyst shows a clear lattice fringe, with the corresponding fringe spacing of 0.336 nm, ascribed to the (002) facet of the CdS nanowires, consistent with the XRD results [48]. Element mapping results from EDS (Fig. 3(m-o)) verified the close

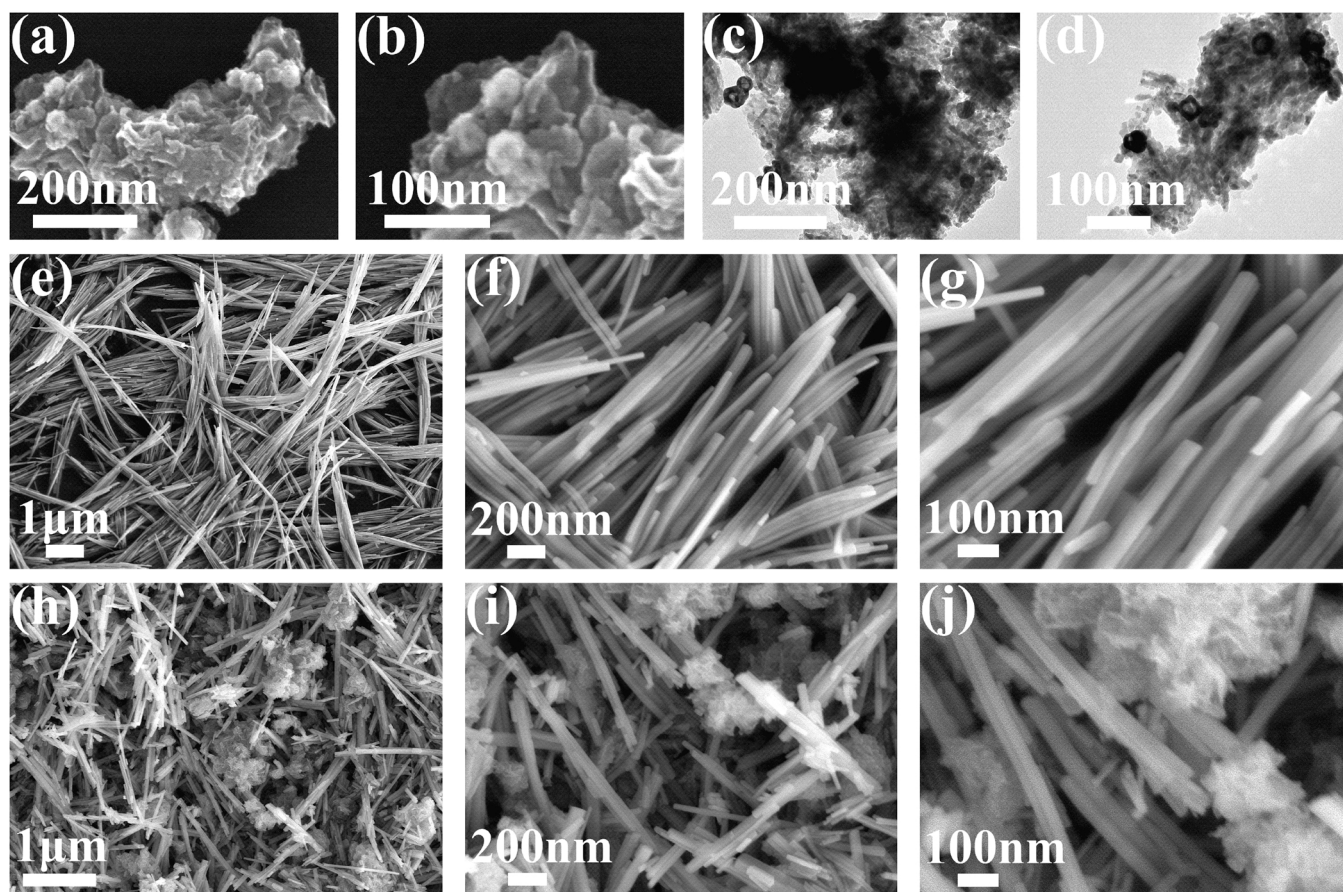
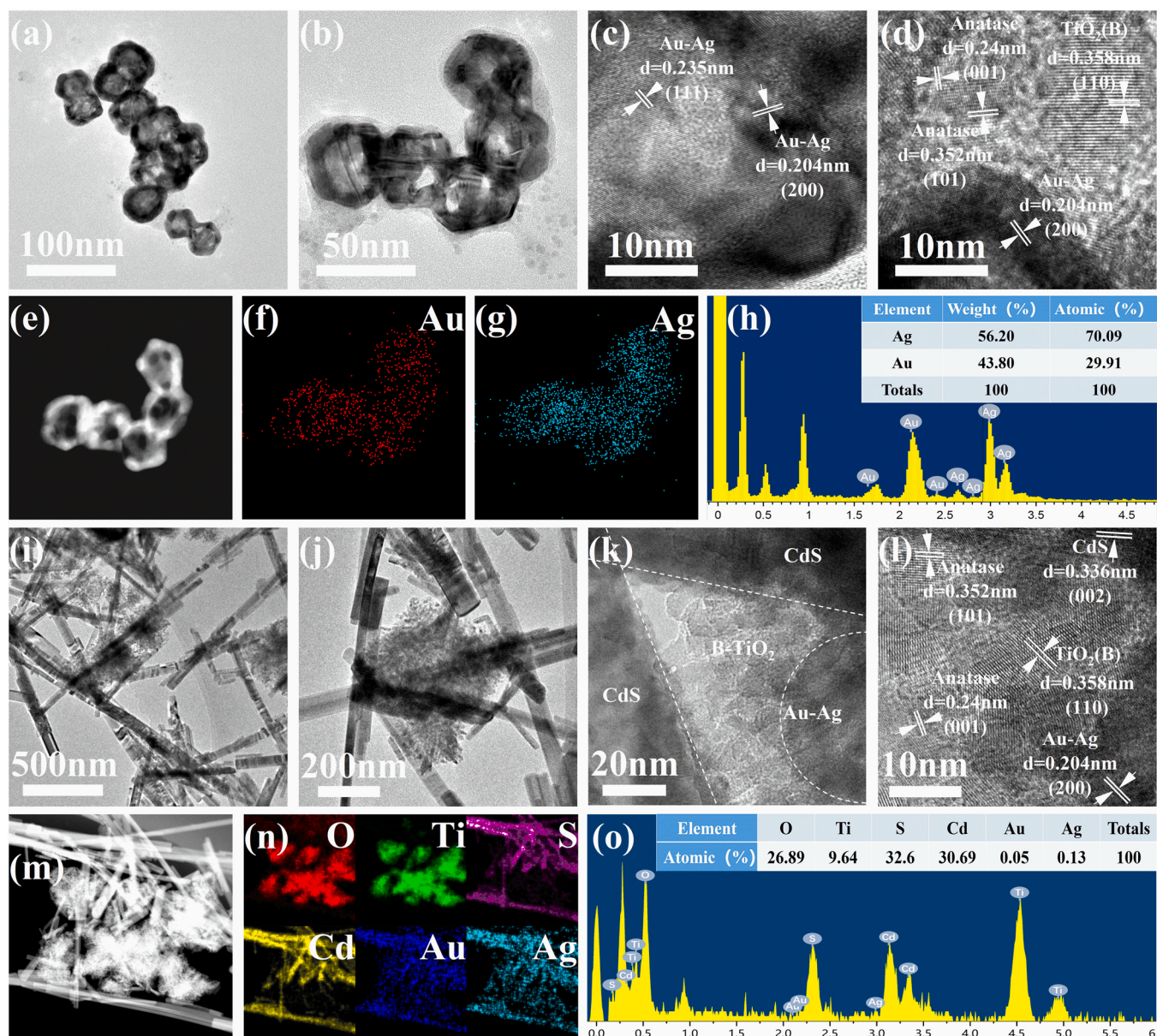


Fig. 2. The morphology images of (a-d) Au-Ag/B- $\text{TiO}_2$ . SEM images of (e-g) the CdS nanowires, and (h-j) the sample CdS/Au-Ag/B- $\text{TiO}_2$ .





**Fig. 3.** (a), (b) TEM images of the Au-Ag alloy. HRTEM images of (c) the Au-Ag alloy, and (d) the Au-Ag/B-TiO<sub>2</sub>. (e-h) Images of HAADF-STEM and EDS mapping for the Au-Ag alloy. (i) (j) TEM images of the CdS/B-TiO<sub>2</sub>. (k) (l) HRTEM images of the CdS/B-TiO<sub>2</sub>. (m-o) Merged images of HAADF-STEM and EDS mapping for the CdS/B-TiO<sub>2</sub>.

contact between the Au-Ag NPs and the B-TiO<sub>2</sub> or the CdS nanowires. Meanwhile, the O, Ti, S, Cd, Au, and Ag were uniformly distributed in the CdS/B-TiO<sub>2</sub>, confirming the formation of the CdS/Au-Ag/B-TiO<sub>2</sub> heterojunction [38]. Therefore, the Au-Ag NPs played a significant role in determining the mobility of the charge carriers, which is responsible for the improved photocatalytic activity of CdS/Au-Ag/B-TiO<sub>2</sub> [41].

### 3.2. Energy band structure and mechanism

Optical properties are important in influencing photocatalytic performance. The optical absorption spectra were measured by UV-Vis DRS to determine the band gaps, as shown in Fig. 4(a). The absorption edge of TiO<sub>2</sub>(B) was around 375 nm, while that of anatase was around 420 nm. The corresponding band gaps were 3.6 eV and 3.2 eV, respectively (Fig. 4(b)), which agrees with previously reported values. Hence, TiO<sub>2</sub> samples only exhibit a UV light response. A redshift of the absorption edge of B-TiO<sub>2</sub> is revealed after the high-temperature hydrogen reduction of TiO<sub>2</sub>. The color of B-TiO<sub>2</sub> changed from white to black

(Fig. 4(d)), and visible light responsiveness was significantly enhanced due to the presence of oxygen vacancies and Ti<sup>3+</sup>. The small peaks at 540 and 675 nm of Au-Ag/B-TiO<sub>2</sub> in the inset may be caused by the LSPR effect of the Au-Ag NPs, assigned to the quadrupole and dipole plasmon signals [18,49]. These characteristic peaks are not particularly obvious due to the low content of the Au-Ag NPs. Fig. 4(a) shows a broadened and slightly enhanced light absorption edge of Au-Ag/B-TiO<sub>2</sub> compared with B-TiO<sub>2</sub>, indicating that the Au-Ag NPs form additional states within the band gap [50], effectively reduce the band gap, and improve the absorption of visible light.

The additional states can also promote charge transfer. The electrons at the top of the valence band can transfer to the Au-Ag state within the band gap [48]. Since the plasmonic bands of the Au-Ag NPs are mainly located in the vis-spectral range overlapped with the B-TiO<sub>2</sub>, the RET mechanism can be valid [51,52], resulting in enhanced visible light absorption, charge carrier generation, and effective charge separation [45]. Therefore, the combination of Au-Ag/B-TiO<sub>2</sub> can significantly enhance the utilization of visible light and generate more charge



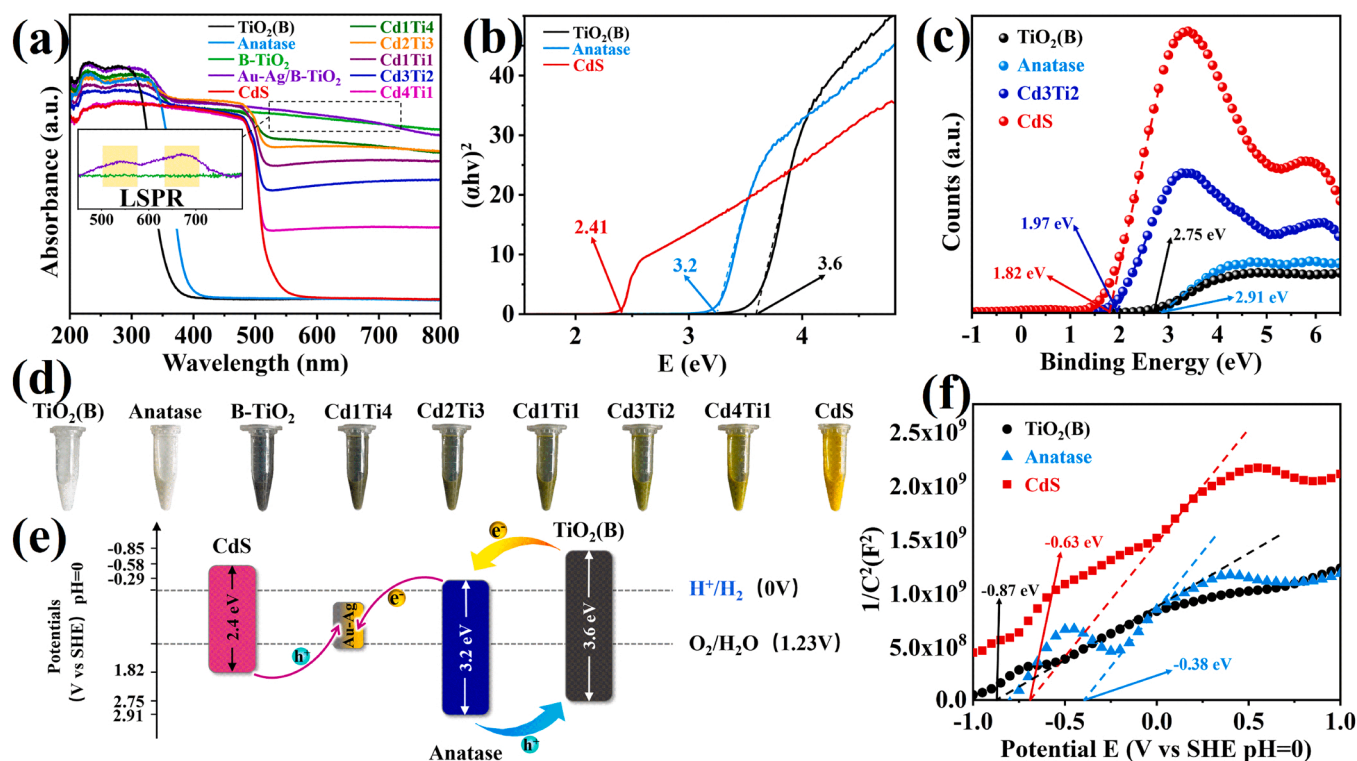


**Fig. 4.** (a) UV-Vis absorption spectra of  $\text{TiO}_2(\text{B})$ , anatase,  $\text{B-TiO}_2$ ,  $\text{Au-Ag/B-TiO}_2$ ,  $\text{CdS}$  and composite catalysts  $\text{CdS/Au-Ag/B-TiO}_2$ , and (b) the absorption spectra from Kubelka-Munk transformed functions. (c) XPS valence band spectra of  $\text{TiO}_2(\text{B})$ , anatase,  $\text{CdS}$  and composite catalysts. (d) Color of the samples. (e) The electronic band structure of  $\text{CdS/Au-Ag/B-TiO}_2$ . (f) Mott-Schottky plots of  $\text{TiO}_2(\text{B})$ , anatase and  $\text{CdS}$ .

carriers.

Fig. 4(a) shows the absorption edge of pure  $\text{CdS}$  nanowires at approximately 530 nm with a corresponding bandgap of 2.41 eV. By coupling  $\text{CdS}$  with  $\text{Au-Ag/B-TiO}_2$ , the light absorption edges of composite catalysts,  $\text{Cd1Ti4}$ ,  $\text{Cd2Ti3}$ ,  $\text{Cd1Ti1}$ ,  $\text{Cd3Ti2}$ , and  $\text{Cd4Ti1}$ , show regular changes. It is worth noting that the absorption edges of the composite catalysts are larger than those of  $\text{B-TiO}_2$  and  $\text{CdS}$ . The results showed that combining  $\text{B-TiO}_2$  and  $\text{CdS}$  could compensate for each other to improve their visible light absorption [39].

To investigate the valence band edge potentials of the catalysts and understand the influence of the band structure on the photocatalytic activity, the valence band edges of  $\text{TiO}_2(\text{B})$ , anatase, and  $\text{CdS}$  were determined by XPS valence band spectroscopy. Fig. 4(c) shows the valence band maxima (VBM) of  $\text{TiO}_2(\text{B})$ , anatase, and  $\text{CdS}$  catalysts that occurred at 2.75 eV, 2.91 eV, and 1.82 eV, respectively. Hence, the corresponding conduction band minima of  $\text{TiO}_2(\text{B})$ , anatase, and  $\text{CdS}$  catalysts are determined to be  $-0.85$ ,  $-0.29$ , and  $-0.58$  V, respectively [48]. The electronic band structure alignments are presented in Fig. 4(e). It shows the influence of introducing  $\text{Au-Ag}$  NPs on the energy band structure of  $\text{TiO}_2(\text{B})$ , anatase, and  $\text{CdS}$  catalysts. The  $\text{CdS/Au-Ag/B-TiO}_2$  composite catalyst exhibits a tandem of type II and type Z heterojunction. The  $\text{Au-Ag}$  NPs act as an electron-transporting medium. UV and partially visible light can be absorbed and excite the  $\text{B-TiO}_2$ , containing both  $\text{TiO}_2(\text{B})$  and anatase, to generate the electron-hole pairs. The separation of these excited charges is improved by the type II heterojunction formed between  $\text{TiO}_2(\text{B})$  and anatase. Meanwhile,  $\text{CdS}$  can absorb visible light to produce excited electrons and holes. The holes in the  $\text{CdS}$  can recombine with the excited electrons transferred from the anatase through  $\text{Au-Ag}$  NPs while retaining its high-energy electrons on the conduction band of the  $\text{CdS}$  for the photocatalytic reaction. In addition, the visible light irradiation activates the surface plasmon of  $\text{Au-Ag}$  NPs. The RET process can effectively promote the generation and separation of the electron-hole pairs, which is favorable for the HER and  $\text{CO}_2\text{RR}$  reactions under sunlight [20].

Mott-Schottky plots were also used to reveal the energy band structure by identifying the flat band potentials of  $\text{TiO}_2(\text{B})$ , anatase and  $\text{CdS}$  catalysts to verify the possible photocatalytic mechanism [53]. The results are shown in Fig. 4(f). All samples were identified as n-type semiconductors due to the positive slopes in the Mott-Schottky plots. The CB of an n-type semiconductor is usually about 0.1 V below the flat band potential [43]. Consequently, the  $E_{\text{fb}}$  (vs. SHE) of  $\text{TiO}_2(\text{B})$ , anatase, and  $\text{CdS}$  were determined to be  $-0.87$ ,  $-0.38$ , and  $-0.63$  V<sub>SHE</sub>, which is close to the results from the XPS-VB and UV-Vis measurements [54, 55]. Therefore, the synergistic effect of the heterojunction electron transfer mechanism and the RET mechanism for improved visible light absorption can improve the efficiency of sunlight utilization to a certain extent, and provide reliable performance for the photocatalytic hydrogen evolution reaction and carbon dioxide reduction reaction.

### 3.3. Identification of chemical bond

To explore the surface composition and chemical states of elements and to confirm the charge transfer mechanism in the  $\text{CdS/Au-Ag/B-TiO}_2$  heterojunction, XPS spectra of  $\text{TiO}_2(\text{B})$ , anatase,  $\text{Au-Ag/B-TiO}_2$ ,  $\text{Cd3Ti2}$ , and  $\text{CdS}$  were analyzed. The survey XPS spectral in Fig. 5(a) verifies the existence of Ti, O, Cd, S, Au, Ag, and C elements, in accord with the result of EDS. The atomic percentages of the elements are listed in Table S1. All samples are pure and free from other impurities. Fig. 5(f) displays the C 1s peaks at 284.8 eV, attributed to surface contaminated carbon, which was used to calibrate the binding energies of all elements. Fig. 5(b) shows the Au 4f spectrum from  $\text{Au-Ag/B-TiO}_2$  with two main peaks at 83.98 and 87.69 eV, assigned to the surface Au species [56]. The peaks at 367.95 and 374.02 eV in Fig. 5(c) are assigned to the Ag [57]. After loading  $\text{CdS}$ , the relative contents of Au and Ag in the composite sample of  $\text{Cd3Ti2}$  decreased (Table S1), as shown in Fig. 5(b) and (c). Spectra from  $\text{TiO}_2(\text{B})$ , anatase,  $\text{Au-Ag/B-TiO}_2$ , and  $\text{Cd3Ti2}$  show symmetrical Ti 2p doublets from  $\text{Ti}^{4+}$  ions (Fig. 5(d)). Two additional peaks from the  $\text{TiO}_2(\text{B})$  at 463.42 and 457.98 eV are ascribed to the  $\text{Ti}^{3+}$

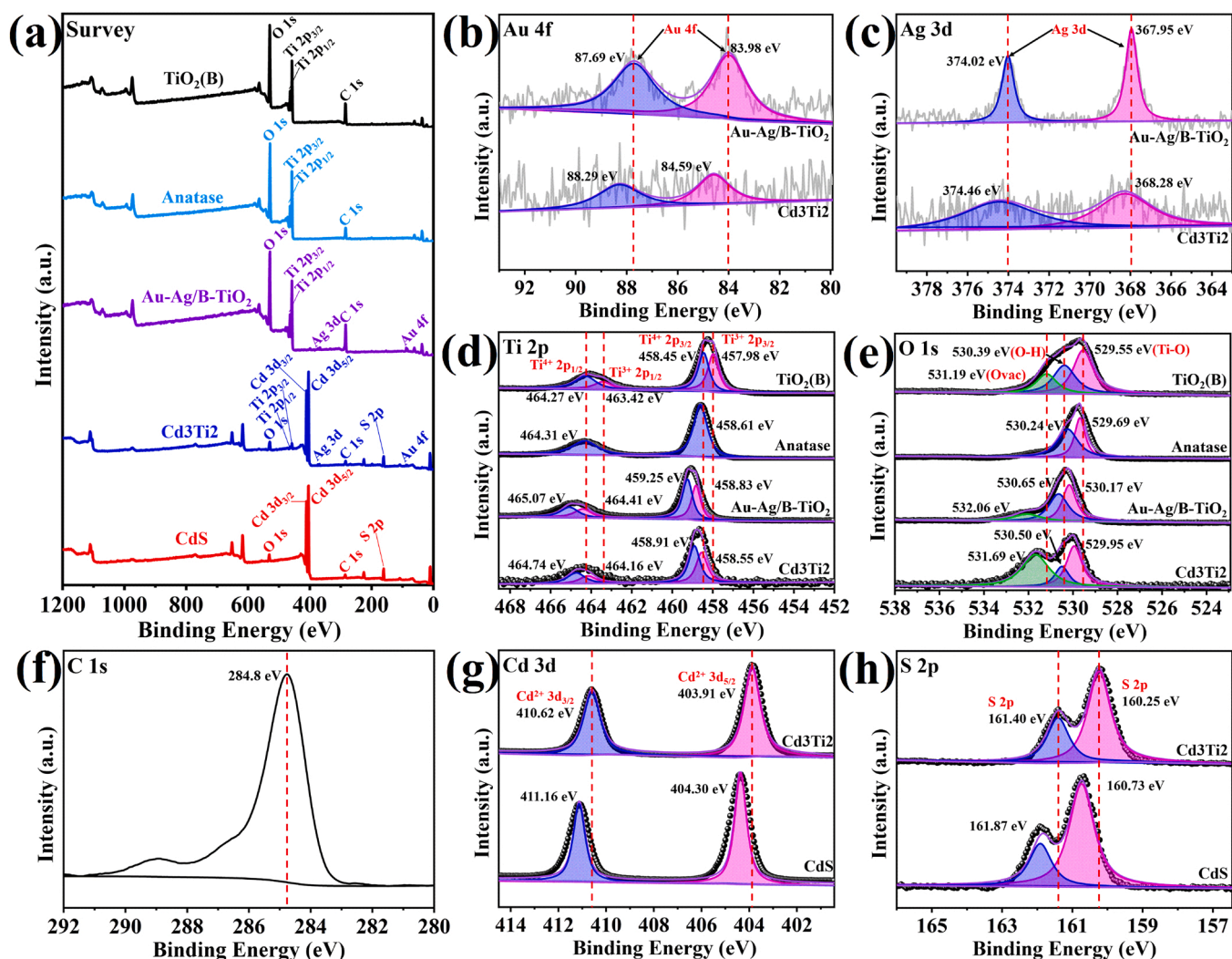


**Fig. 5.** (a) XPS survey spectra for  $\text{TiO}_2(\text{B})$ , anatase, Au-Ag/B- $\text{TiO}_2$ ,  $\text{Cd}_3\text{Ti}_2$  and CdS. (b) The high resolution XPS spectra of Au 4f, (c) Ag 3d, (d) Ti 2p, (e) O 1s, (f) C 1s, (g) Cd 3d, (h) S 2p.

$2p_{1/2}$  and  $\text{Ti}^{3+} 2p_{3/2}$ , respectively. The O 1s spectrum from  $\text{TiO}_2(\text{B})$  is shown in Fig. 5(e), with three peaks at 529.55, 530.39, and 531.19 eV, which are assigned to the lattice oxygen (Ti-O), the adsorbed oxygen (O-H) [46], the abundant oxygen vacancies (Ovac) [45]. For the anatase obtained from calcining  $\text{TiO}_2(\text{B})$  at 550 °C in air, the Ovac peak disappeared in Fig. 5(d) and (e). Meanwhile, the hydrogen reduction at high temperatures inhibited the formation of defects-free anatase while retaining the density of oxygen defects.

For the Au-Ag/B- $\text{TiO}_2$  composite, the two  $\text{Ti}^{4+} 2p$  peaks are shifted to 465.07 and 459.25 eV, respectively. According to the previous report, the electron concentration can increase when the bond is formed between the two-phase interfaces [45]. Both the Ti 2p and the O 1s binding energies are shifted to higher binding energies compared with  $\text{TiO}_2(\text{B})$  (Fig. 5(d) (e)). This indicates a reduced electron density in  $\text{TiO}_2(\text{B})$ , suggesting that the photo-generated electrons transfer from  $\text{TiO}_2(\text{B})$  to anatase, and are further extracted by Au Ag alloy. At the same time, the  $\text{Cd}_3\text{Ti}_2$  heterojunction composite displayed negative shiftings in the binding energies of  $\text{Ti}^{4+} 2p$  (−0.34 eV) and O 1s (−0.22 eV), demonstrating that the multielement  $\text{Cd}_3\text{Ti}_2$  heterojunction has the strong interaction, which is conducive the transfer of photoinduced carriers [39,48,58]. The Cd 3d binding energies from the composite  $\text{Cd}_3\text{Ti}_2$  at 410.62 and 403.91 eV are assigned to the Cd  $3d_{3/2}$  and  $3d_{5/2}$ , respectively (Fig. 5(g)). These peaks are redshifted to the lower binding energies than Cd 3d in CdS (411.16 and 404.30 eV). Meanwhile, the

binding energy of S 2p shows similar shifts (Fig. 5(h)). Such shifts might be due to the difference in the work functions at the interface, causing charge transfer at the heterojunction interface, with the CdS as the electron acceptor [44].

Meanwhile, the binding energies of Au and Ag in their high-resolution XPS spectra in the  $\text{Cd}_3\text{Ti}_2$  heterojunction shift towards the higher binding energies in comparison with that of Au-Ag/B- $\text{TiO}_2$ , suggesting that the Au-Ag NPs are the electron donor. Due to the high CB position of the CdS (Fig. 4(e)), it is not conducive to the flow of the electrons from Au-Ag NPs to CdS, which indicates that the heterojunction system follows a Z mechanism. The result substantiates that the electrons migrate from the B- $\text{TiO}_2$  component to the Au-Ag alloy under the light irradiation, the low-energy photo-generated holes from CdS combine with low-energy photo-generated electrons gathered on the Au-Ag alloy, while the high-energy photo-generated electrons on CdS participate in the reaction, which is consistent with the proposed charge transfer mechanism [59].

### 3.4. Photoelectrochemical measurements

The photocatalytic properties of CdS/Au-Ag/B- $\text{TiO}_2$  composites are further explored by the transient photocurrent responses and electrochemical impedance spectroscopy (EIS). As shown in Fig. 6(a), The photocurrent response of pure  $\text{TiO}_2(\text{B})$  is very weak, which is caused by



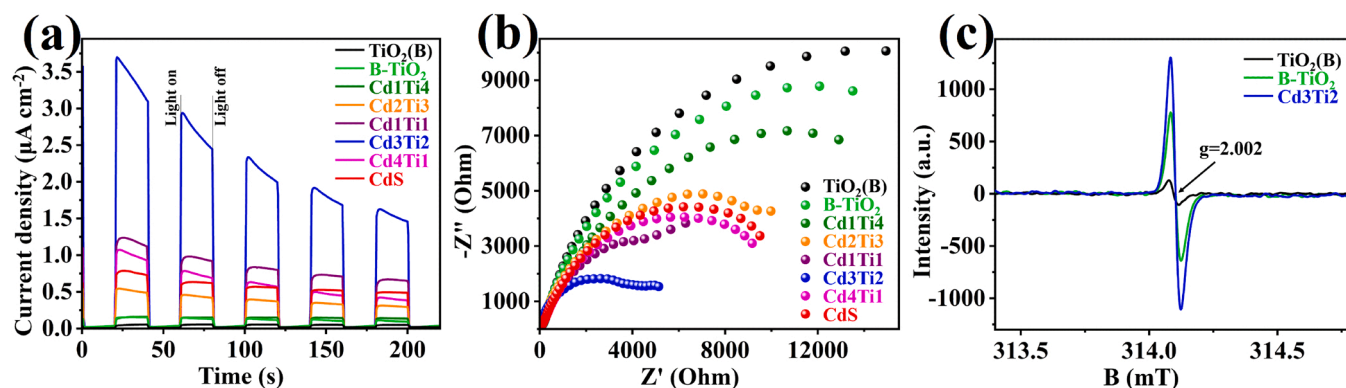


Fig. 6. (a) Transient photocurrent responses for  $\text{TiO}_2(\text{B})$ , B-TiO<sub>2</sub>, CdS and composite catalysts CdS/Au-Ag/B-TiO<sub>2</sub>, and (b) The electrochemical impedance spectra (EIS). (c) Electron paramagnetic resonance (EPR) of  $\text{TiO}_2(\text{B})$ , B-TiO<sub>2</sub> and Cd3Ti2.

the poor response to visible light and fast charge recombination. The photocurrent intensity of the CdS/Au-Ag/B-TiO<sub>2</sub> composites has been greatly improved. In particular, the average value of photocurrent intensity of 2.13  $\mu\text{A cm}^{-2}$  on the Cd3Ti2, which is about 42 times that on the pristine  $\text{TiO}_2(\text{B})$  and 3.8 times that on CdS. Hence, the heterojunction structures of Cd3Ti2 can effectively separate photo-generated electron and hole pairs to improve photocatalytic performance [46]. In addition, the near-field electromagnetic coupling of the Au Ag plasma also plays an important role, which showed that the rate of electron-hole formation in semiconductors  $\text{TiO}_2$  and CdS was enhanced in the regions near the Au Ag NPs with excited plasmonic effects [25].

Meanwhile, the electrochemical impedance spectroscopy (EIS) measurements are shown in Fig. 6(b) to illustrate the electron transfer process. The semicircle radius of Cd3Ti2 is smaller than those of other samples, implying less interface resistance for carrier transfer due to the enhanced electron mobility, which agrees with the photocurrent results [43,45]. All this data together identifies the fast electron transferring in Cd3Ti2, implying a promoted charge separation owing to the formation of a heterojunction [39,60].

To confirm the improved charge separation, the PL spectra of  $\text{TiO}_2(\text{B})$ , CdS, and Cd3Ti2 in the range of 360–500 nm are collected and shown in Fig. S6. Since the PL emission results from charge recombination, a lower PL intensity generally indicates a higher charge separation efficiency [60]. The PL emission peak intensity of  $\text{TiO}_2(\text{B})$  is the highest in the testing samples, implying the highest electron-holes recombination rate. On the contrary, Cd3Ti2 has the lowest PL intensity, evidencing effective inhibition of the charge recombination, which is consistent with the results of the photocurrent responses and EIS measurements [43]. Therefore, the multiple heterojunction structures and the RET mechanism can efficiently promote the separation and transportation of electron-hole pairs and inhibit their recombination.

Electron paramagnetic resonance (EPR) has been widely used to reveal the existence of Ovac directly. As shown in Fig. 6(c), a significant EPR signal with a g value of 2.002 is observed in the samples of  $\text{TiO}_2(\text{B})$ , B-TiO<sub>2</sub>, and Cd3Ti2, which indicates the existence of Ovac accompanied with the  $\text{Ti}^{3+}$  in these samples, which is in good agreement with the XPS results [38]. Further comparison in the intensities of the EPR signals revealed that the B-TiO<sub>2</sub> and Cd3Ti2 have higher Ovac concentrations than the  $\text{TiO}_2(\text{B})$ , proving that high temperature hydrogen reduction can significantly promote the production of  $\text{Ti}^{3+}$  and Ovac. The existence of  $\text{Ti}^{3+}$  and Ovac is significant for improving photocatalytic performance.

### 3.5. Photocatalysis performance

Photocatalytic performance is evaluated to reveal the advantages of the catalytic system. Here, two of the most common photocatalytic reactions, the photocatalytic HER reaction and the photocatalytic CO<sub>2</sub>RR reaction, were carried out. The photocatalytic hydrogen evolution

properties of CdS/Au-Ag/B-TiO<sub>2</sub> composites were assessed under the full solar spectrum (AM=1.5). The photocatalytic hydrogen evolution performances of pristine  $\text{TiO}_2(\text{B})$  and CdS were also examined under identical reaction conditions. The photocatalytic hydrogen evolution amount versus irradiation time over the CdS/Au-Ag/B-TiO<sub>2</sub>,  $\text{TiO}_2(\text{B})$ , and CdS are plotted in Fig. 7(a). The amount of the produced  $\text{H}_2$  was linearly increased with the reaction time. Accordingly, the reactivities of CdS/Au-Ag/B-TiO<sub>2</sub> with different contents of CdS are better than  $\text{TiO}_2(\text{B})$  and CdS. Results confirmed the superior activity of Cd3Ti2, achieving an  $\text{H}_2$  production rate of 15.97  $\text{mmol}\cdot\text{h}^{-1}\cdot\text{g}^{-1}$ , which is 24.2 times higher than that of the  $\text{TiO}_2(\text{B})$  (0.66  $\text{mmol}\cdot\text{h}^{-1}\cdot\text{g}^{-1}$ ), and 17.9 times higher than that of CdS (0.89  $\text{mmol}\cdot\text{h}^{-1}\cdot\text{g}^{-1}$ ), respectively (Fig. 7 (b)). The obtained apparent quantum efficiency (AQE) of Cd3Ti2 at 365 nm and 420 nm are 10.6% and 1.7%, respectively. The AQE of CdS, B-TiO<sub>2</sub>, and Cd3Ti2 under different wavelengths of monochromatic light irradiation are summarized in Table S2.

The excellent HER performance of Cd3Ti2 could be attributed to the following aspects. Firstly, high-temperature hydrogen reduction improves the visible light absorption of  $\text{TiO}_2(\text{B})$ ; secondly, the synergy of the type II heterojunction and the Z-type heterojunction greatly inhibits the recombination of the electron-hole pair; besides, the Au-Ag NPs between the  $\text{TiO}_2$  and CdS form a strong localized surface plasmon resonance (LSPR). Among them, the LEMF mechanism further enhances the charge transfer of the Z-type heterostructures. The RET mechanism also enhances the charge carrier generation and separation. Comparing related reports on the plasma mediated photocatalysis of hydrogen production (Table S3), the CdS/Au-Ag/B-TiO<sub>2</sub> produced in this work offers the best HER performance. To further demonstrate the superiority of Au-Ag alloy, we replaced the Au-Ag alloy in the CdS/Au-Ag/B-TiO<sub>2</sub> with Ag nanoparticles. The photocatalytic performance of CdS/Au-Ag/B-TiO<sub>2</sub> and CdS/Ag/B-TiO<sub>2</sub> are compared in Fig. S7. The Au-Ag alloy in the CdS/Au-Ag/B-TiO<sub>2</sub> system was more beneficial to the photocatalytic performance than the pure Ag nanoparticles. Cycling photocatalytic hydrogen evolution experiments were carried out to study the stability of the Cd3Ti2 HER performance [39]. As shown in Fig. 7(c), the  $\text{H}_2$  production rate of Cd3Ti2 maintains fairly constant during 12 cycles of reaction, decreasing slightly to 81.3%, indicating good stability of Cd3Ti2 [43]. The Cd3Ti2 is subjected to morphological observation after long-cycle experiments, as shown in Fig. S8, and no significant changes in its structure occurred. We speculate that the photocorrosion of CdS is the main cause of the performance degradation in the Cd3Ti2.

The performances of the various photocatalysts for CO<sub>2</sub> reduction were evaluated under the full solar spectrum (AM=1.5). As shown in Fig. 8(a) and (b), the main products of the reaction are CH<sub>4</sub> and CO [61–63]. Both  $\text{TiO}_2(\text{B})$  and CdS showed low photocatalytic activities toward CO<sub>2</sub> reduction. Interestingly, the heterojunction photocatalyst of CdS/Au-Ag/B-TiO<sub>2</sub> showed a significantly improved activity for CO<sub>2</sub> reduction [46]. The photocatalytic activity can be optimized by

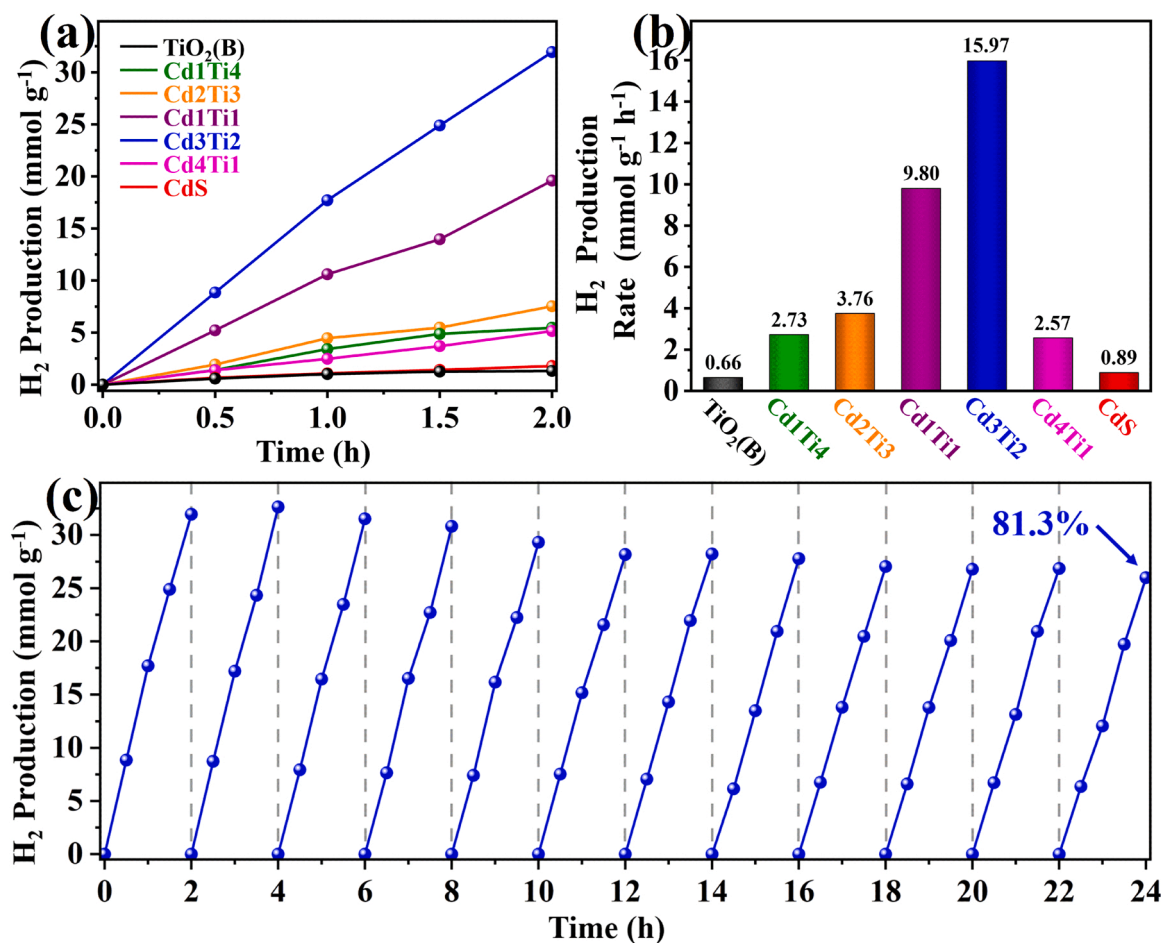


Fig. 7. Photocatalytic hydrogen evolution reaction (HER). (a) H<sub>2</sub> production under simulated solar irradiation of TiO<sub>2</sub>(B), CdS and composite catalysts CdS/Au-Ag/B-TiO<sub>2</sub>, and (b) Corresponding hydrogen production rates. (c) Stability test of Cd3Ti2 (the reaction system was evacuated for 20 min every 2 h).

adjusting the relative proportions of B-TiO<sub>2</sub> and CdS. As shown in Fig. 8 (c), the photocatalytic activities of the CdS/Au-Ag/B-TiO<sub>2</sub> show slight changes as the mass ratio of CdS to B-TiO<sub>2</sub> increases from 1:4–1:1. However, when the mass ratio of CdS to B-TiO<sub>2</sub> exceeded 1:1, the CO<sub>2</sub> reduction rates begin to improve significantly [58]. Among all composite photocatalysts, samples Cd3Ti2 and Cd4Ti1 exhibited the optimal CH<sub>4</sub> and CO production rates, respectively. The Cd3Ti2 shows the highest CH<sub>4</sub> yield rate of 14.2 μmol·h<sup>-1</sup>·g<sup>-1</sup>, and is almost 15.8 times the yield from CdS (CH<sub>4</sub> production activity was not detected in TiO<sub>2</sub>(B)). The Cd4Ti1 shows the highest CO yield of 327.2 μmol·h<sup>-1</sup>·g<sup>-1</sup>, almost 5.4 and 36 times the yields from TiO<sub>2</sub>(B) and CdS, respectively [64]. The reactions producing CH<sub>4</sub> and CO involve 8 and 2 electrons, respectively. For the Cd3Ti2, the CH<sub>4</sub> content accounts for 11.1% (Fig. 8(d)), and CO is the main product of the CO<sub>2</sub>RR reaction. The literature results of plasma mediated photocatalytic CO<sub>2</sub> reduction are compared in Table S4. According to the above analysis, the combination of Type II and Z-Type composite heterojunctions, RET and LEMF mechanisms has improved the directional charge transfer kinetics, resulting in the high performance of photocatalytic carbon dioxide reduction and HER.

### 3.6. Finite-difference time-domain (FDTD) simulations

The internal mechanism of the Au-Ag NPs LSPR effects on the photocatalytic performance of CdS/Au-Ag/TiO<sub>2</sub> is investigated using the FDTD simulation to study the LEMF mechanism, as shown in Fig. 9. A hot spot representing the focused electromagnetic field is identified in the junction under the excitation of a 520 nm light polarized along the X-axis. The electromagnetic intensity of the local hot spot is much higher

than that of the far-field excitation light, where the strength of the electromagnetic field is at least one order of magnitudes higher than that of the far-field excitation light [65]. The carrier generation and separation rates in the hot spot region will significantly increase. The results show that the Au-Ag NPs in the CdS/Au-Ag/TiO<sub>2</sub> effectively increase the electromagnetic field intensity, especially at the interfaces around the Au-Ag NPs interfaced with CdS or TiO<sub>2</sub>. Quantitatively, the electromagnetic field enhancements from the Au-Ag NPs, CdS/Au-Ag, and Au-Ag/TiO<sub>2</sub> are 1.3, 9, and 8.6, respectively. This means that the electromagnetic fields for CdS/Au-Ag or Au-Ag/TiO<sub>2</sub> are about 1 order of magnitude higher than that of Au-Ag NPs, indicating the importance of the heterojunction structure formed between Au-Ag NPs and the coupled semiconductors of CdS and TiO<sub>2</sub>. In conventional semiconductor-metal-semiconductor Z-type heterojunctions, low-energy electrons and low-energy holes recombine at the metallic components, thereby retaining high-energy electrons and holes for redox reactions. It is speculated that the strong electromagnetic field of the Au-Ag NPs will accelerate the transfer and combination of the low-energy electrons and holes in the electromagnetic field while suppressing the recombination of the high-energy electrons and holes, as confirmed by the EPR results. In summary, the intense plasmonic EM field at the metal nanostructures can significantly increase the interband transition rate in the adjacent semiconductors and facilitate the separation of photo-generated electron-hole pairs [18,22].

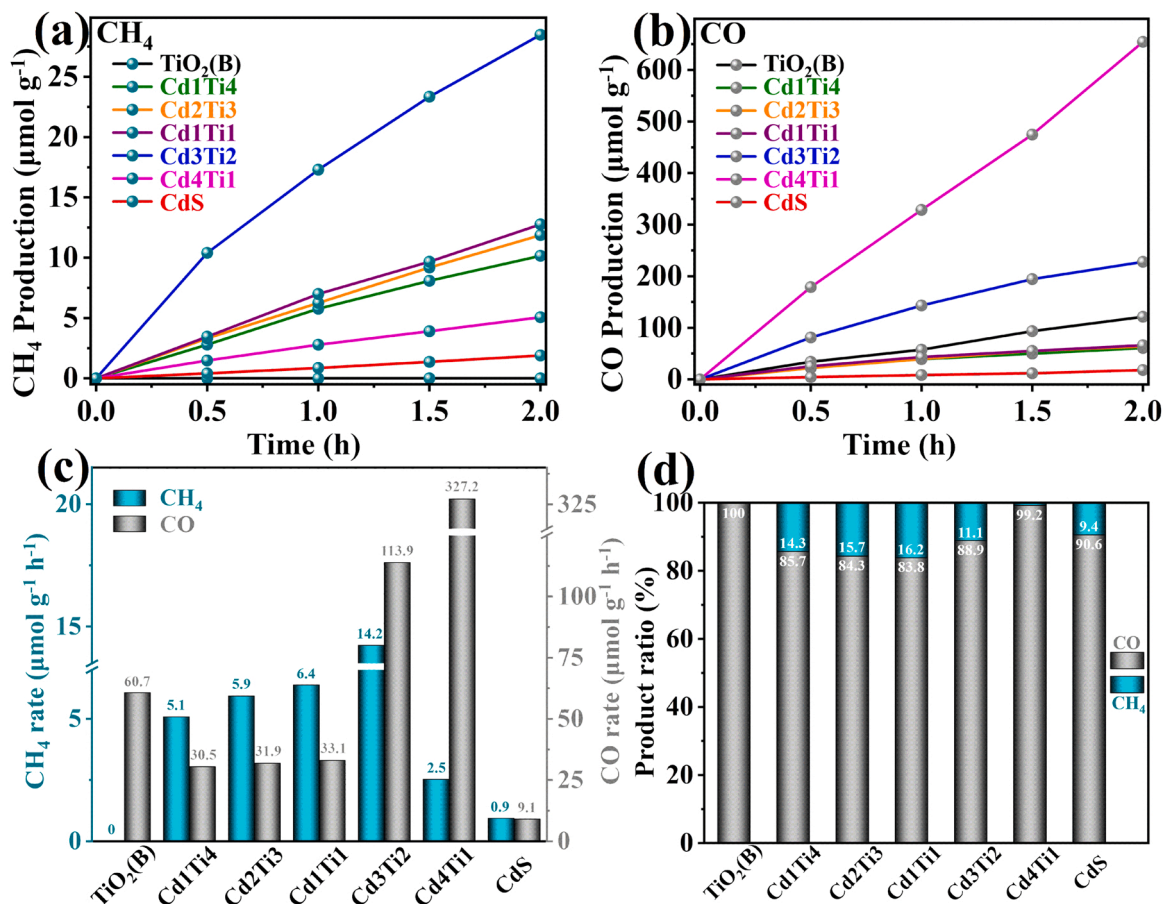


**Fig. 8.** Photocatalytic Carbon dioxide reduction reaction (CO<sub>2</sub>RR). (a) CH<sub>4</sub> production under simulated solar irradiation of TiO<sub>2</sub>(B), CdS and composite catalysts CdS/Au-Ag/B-TiO<sub>2</sub>, and (b) CO production, and (c) Corresponding production rates of CH<sub>4</sub> and CO, and (d) The distribution of carbon dioxide reduction products.

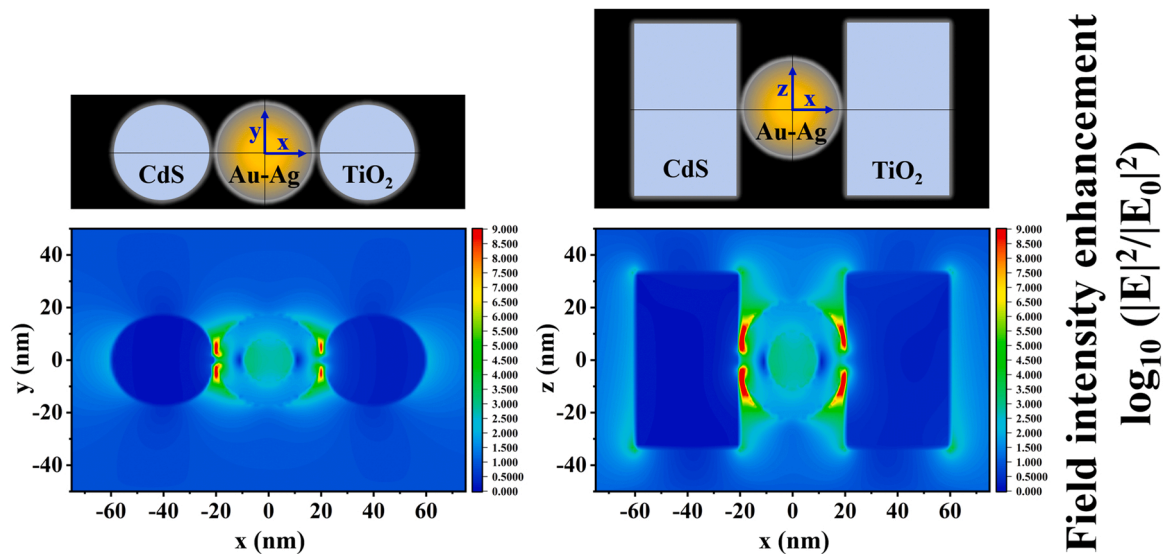


**Fig. 9.** Electric field profile for CdS/Au-Ag/TiO<sub>2</sub> in the substrate (xy) plane and (xz) plane. The incident plane wave is polarized in the x-direction and propagates along the z-direction.

### 3.7. Density functional theory (DFT) calculations

#### 3.7.1. Structure Information

Combining the elemental analysis (XPS and EDS) with our previous work [26,27], the element ratio of Au-Ag NPs can be obtained as 3:7. To

calculate the electronic structures of the CdS/Au<sub>3</sub>Ag<sub>7</sub>/TiO<sub>2</sub> photocatalyst, we first built a three-layers Ag (111) with 3 × 3 supercell, and contain 27 Ag atoms. To simulate the Au<sub>3</sub>Ag<sub>7</sub>, eight Ag is replaced by Au, distributed uniformly. The lattice parameter is 8.65, 8.65, and 29.71 Å. CdS (002) is built by six layers with 2 × 2 supercell, including a



vacuum layer of 15 Å with the lattice parameter of 8.41, 8.41, and 22.68 Å. Hence, the lattice mismatch ratio is less than 5%. A similar method was used for constructing the  $\text{Au}_3\text{Ag}_7\text{-TiO}_2$  composite, which contains 48 Ti, 80 O, 20 Au, and 52 Ag, as shown in Fig. 10.

### 3.7.2. The electronic structure analysis

DFT calculations provide further insight into the underlying mechanisms. The work function ( $\Phi$ ) is a crucial parameter for electron transfer within heterojunctions, defined by the energy difference between the vacuum and Fermi levels. The work functions of  $\text{Au}_3\text{Ag}_7\text{-CdS}$  and  $\text{Au}_3\text{Ag}_7\text{-TiO}_2$  were calculated to establish the possible migration within the  $\text{CdS/Au}_3\text{Ag}_7\text{/TiO}_2$  material. As shown in Fig. 11 (a) and (d), the calculated work functions of the  $\text{Au}_3\text{Ag}_7\text{-TiO}_2$  and  $\text{Au}_3\text{Ag}_7\text{-CdS}$  are 4.64 and 6.35 eV, respectively. Hence, the  $\text{Au}_3\text{Ag}_7\text{-CdS}$  has a lower Fermi level than the  $\text{Au}_3\text{Ag}_7\text{-TiO}_2$ .

Consequently, the electrons will transfer from the  $\text{Au}_3\text{Ag}_7\text{-TiO}_2$  to  $\text{Au}_3\text{Ag}_7\text{-CdS}$  across their interface to find a balance of Fermi levels. Thus, a built-in electric field was formed at the interface between  $\text{Au}_3\text{Ag}_7\text{-CdS}$  and  $\text{Au}_3\text{Ag}_7\text{-TiO}_2$ , pointing from the  $\text{Au}_3\text{Ag}_7\text{-CdS}$  to  $\text{Au}_3\text{Ag}_7\text{-TiO}_2$ , which drives the migration of the photo-generated electrons and holes. Therefore, it is expected that, with the  $\text{CdS/Au}_3\text{Ag}_7\text{/TiO}_2$  heterojunction excited under sunlight, the low-energy photo-generated charges will be transferred from the  $\text{TiO}_2$  to the Au-Ag NPs. Conversely, the low-energy photo-generated holes will be transferred from the CdS to Ag-Au NPs. After their annihilation, the energetic electrons will be left on the CB of the CdS, while the excited holes will be left on the VB of the  $\text{TiO}_2$ . As

such, the photoexcited charges are well separated[4,66].

DFT calculations were also performed to identify further the electronic structure of the  $\text{CdS/Au}_3\text{Ag}_7\text{/TiO}_2$ . As shown in Fig. 11 (b) and (e), the electron density of the conduction band (CB) of  $\text{Au}_3\text{Ag}_7\text{-TiO}_2$  decreases, whereas the electron density of CB of  $\text{Au}_3\text{Ag}_7\text{-CdS}$  increases (PDOS). This is revealed from the density of state (DOS) and partial density of state (Fig. S9) in Fig. 11 (b) and (e). Fig. S10 shows the electron depletion and accumulation in the  $\text{Au}_3\text{Ag}_7\text{-TiO}_2$  and  $\text{Au}_3\text{Ag}_7\text{-CdS}$ . This proves the existence of strong interactions across the interfaces, eliminating some dangling bonds and generating interfacial electronic states. The electrostatic potential shows an abrupt change along the interface directly with a contact potential difference. In the  $\text{Au}_3\text{Ag}_7\text{-CdS}$  interface, the blue bubbles represent the dissipation of electrons, and the yellow bubbles represent the aggregation of electrons. The interfacial potential difference drives the transfer of photogenerated holes on CdS to the alloy region. Similarly, the opposite process exists at the  $\text{Au}_3\text{Ag}_7\text{-TiO}_2$  interface. This can further enhance the Z-type heterojunction mechanism and improve photocatalytic activity. By forming the  $\text{CdS/Au-Ag/B-TiO}_2$  composite, a strong electrical field is expected to be formed by moving electron density from CdS to  $\text{TiO}_2$ , mediated by Au-Ag. A strong field is essential for the charge separation at the purposely built interfaces. The band structures of  $\text{Au}_3\text{Ag}_7\text{-TiO}_2$  and  $\text{Au}_3\text{Ag}_7\text{-CdS}$  (Fig. 11 (c) and (f)) show that the band structures of both materials certain metallic properties, which benefit the migration of electrons [66].

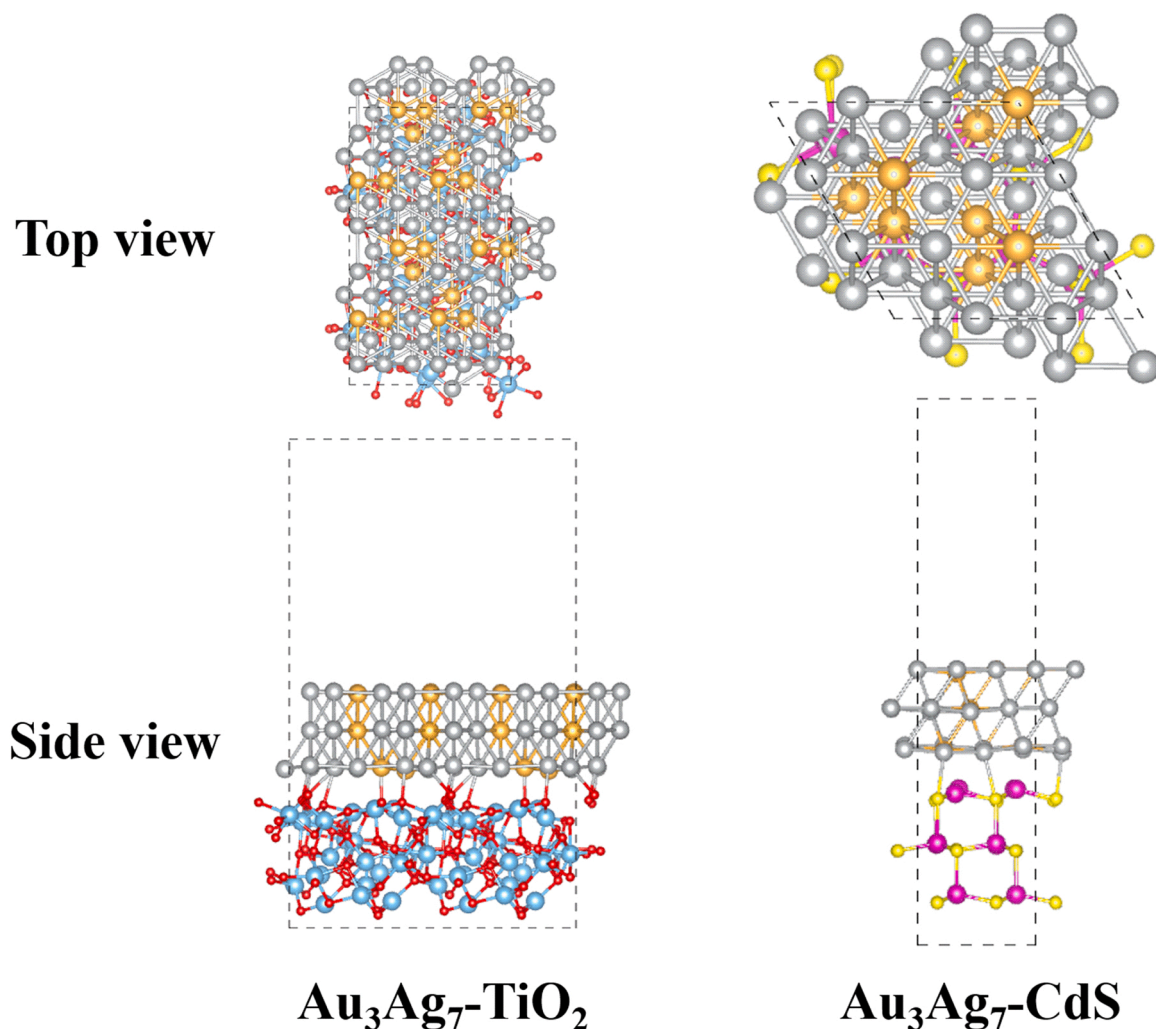
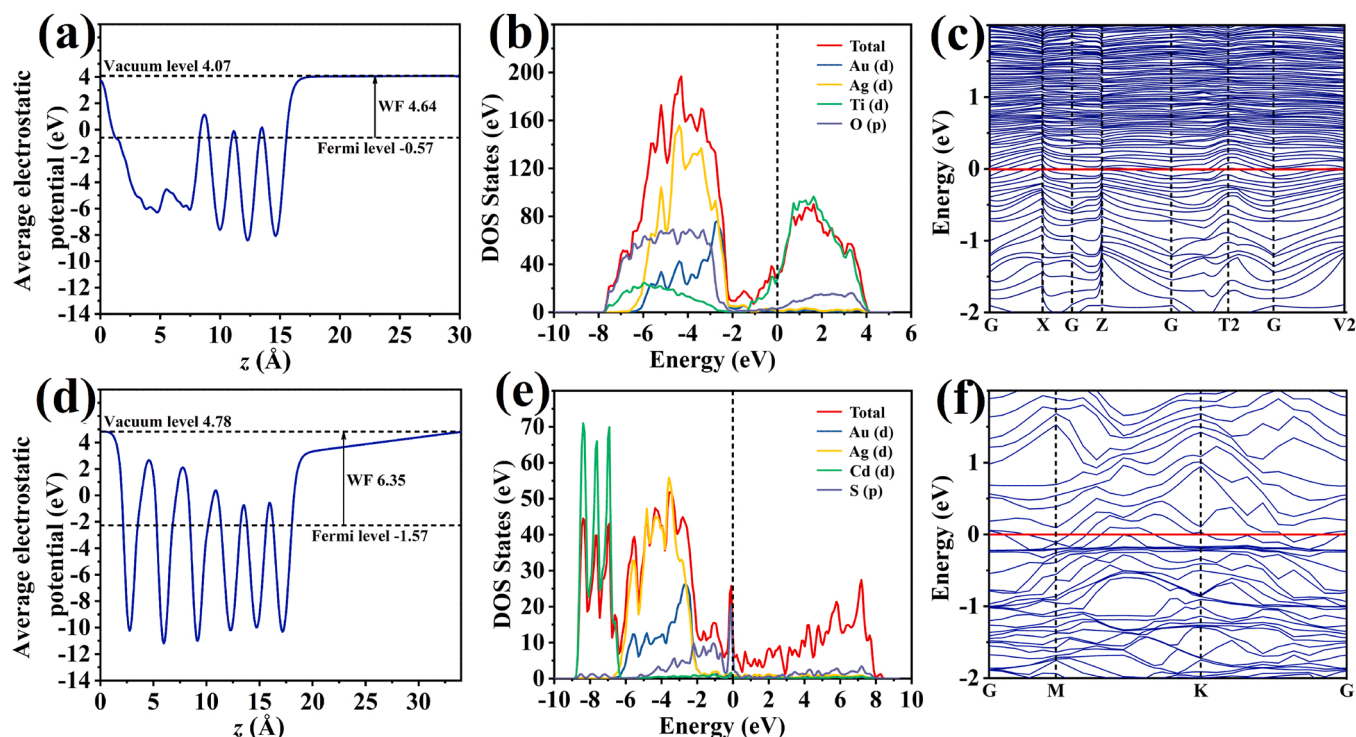


Fig. 10. The optimized structure models of  $\text{Au}_3\text{Ag}_7\text{-TiO}_2$  and  $\text{Au}_3\text{Ag}_7\text{-CdS}$  materials.





**Fig. 11.** (a) Calculated Fermi levels and work functions of  $\text{Au}_3\text{Ag}_7\text{-TiO}_2$ . (b) Density of states and partial density of states for  $\text{Au}_3\text{Ag}_7\text{-TiO}_2$ . (c) Band structure for  $\text{Au}_3\text{Ag}_7\text{-TiO}_2$ . (d) Calculated Fermi levels and work functions of  $\text{Au}_3\text{Ag}_7\text{-CdS}$ . (e) Density of states and partial density of states for  $\text{Au}_3\text{Ag}_7\text{-CdS}$ . (f) Band structure for  $\text{Au}_3\text{Ag}_7\text{-CdS}$ .

### 3.8. Photocatalytic mechanism discussion

The intrinsic mechanism of the  $\text{CdS}/\text{Au-Ag}/\text{B-TiO}_2$  photocatalytic system has been systematically analyzed with using FDTD simulations and DFT calculations [4]. The obtained potentials could be converted into normal hydrogen electrode (NHE) potentials by the following formula:  $E_{\text{NHE}} = E_{\text{AgCl}} + E_{0\text{AgCl}} + 0.059 \text{ pH}$  [48]. Hence, the calculated VB edge positions of the CdS, anatase, and  $\text{TiO}_2(\text{B})$  were estimated to be 1.41, 2.5, and 2.34  $V_{\text{NHE}}$ , while the corresponding CB positions were calculated to be -0.99, -0.7, and -1.26  $V_{\text{NHE}}$  (Fig. 12), which are more negative than the redox potential of  $\text{CO}_2$  reduction to CO ( $\text{CO}_2/\text{CO}$ , -0.53  $V_{\text{NHE}}$ ) and  $\text{CH}_4$  ( $\text{CO}_2/\text{CH}_4$ , -0.24  $V_{\text{NHE}}$ ), implying the photoexcited electrons are negative enough to facilitate the photocatalytic reduction reaction over the  $\text{CdS}/\text{Au-Ag}/\text{B-TiO}_2$  [67].

The Au-Ag alloy nanoparticles play the role of electron mediators in this system, promoting the complexation of low-energy electron and low-energy hole phases in the system, thus improving the utilization of high-energy electrons. Meanwhile, the powerful SPR effect of Au-Ag

alloy promotes this process. Through the RET mechanism, the photoabsorption is not limited by the semiconductor bandgap energy in the full spectrum, and carriers are generated and separated at energy levels above and below the bandgap. Meanwhile, a built-in electric field at the interface between  $\text{Au}_3\text{Ag}_7\text{-CdS}$  and  $\text{Au}_3\text{Ag}_7\text{-TiO}_2$  drives the transfer of low-energy electrons from  $\text{TiO}_2$  to Au-Ag NPs and the low-energy photo-generated holes from CdS to Ag-Au alloy, which are recombined at Au-Ag NPs. Finally, the high-energy photoexcited electrons will stay on the CB of CdS, while the high-energy holes will stay on the VB of  $\text{TiO}_2$ . The photoexcited charges are well separated, verified by the DFT calculations. The strong electromagnetic field on the Au-Ag NPs will accelerate the transfer of the low-energy electrons and holes. The FDTD simulation confirmed the LEMF mechanism. The  $\text{CdS}/\text{Au-Ag}/\text{B-TiO}_2$  composite structure provides two electric fields to drive the charge separation. One is the local electric field generated by LSPR, and the other is the built-in electric field through the interface. The superposition of these two electric fields can significantly improve the photocatalytic performance of the  $\text{CdS}/\text{Au-Ag}/\text{B-TiO}_2$ . In addition, given the complexity of the mechanism, the system mechanism in different wavelength cases should be considered. The Au-Ag alloy absorbs visible light and generates an electromagnetic field by LSPR, so the LEMF, RET mechanism, and Z-type heterojunction electron transfer mechanism operate well in the full spectrum and under visible light ( $\lambda > 420 \text{ nm}$ ) irradiation only. However, the role of Au-Ag alloy in the  $\text{CdS}/\text{Au-Ag}/\text{B-TiO}_2$  system is greatly limited under UV irradiation. Under such conditions, the Au-Ag will serve as an electron transfer mediator.

### 4. Conclusions

In summary, the novel  $\text{CdS}/\text{Au-Ag}/\text{B-TiO}_2$  composite heterojunction was successfully prepared with RET mechanism to improve the visible light photocatalytic performance. The established composite heterojunctions (II-type and Z-type) are responsible for the improved charge separation. Meanwhile, the combined characteristics of the photocatalytic Z-type heterojunction system with a solid electronic medium,

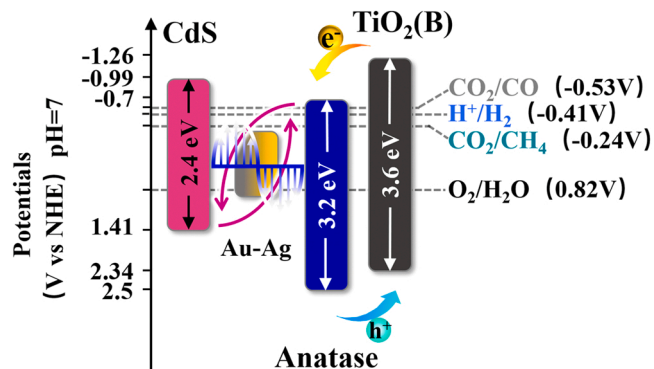


**Fig. 12.** The intrinsic reaction mechanism of the  $\text{CdS}/\text{Au-Ag}/\text{B-TiO}_2$  catalytic system.

bimetallic nanoparticles are used to replace the traditional electronic medium to construct a dual electric field structure with the possible coupling between the electric field at the interface and the plasmon electromagnetic field. Here, two photocatalytic performance tests were performed over the CdS/Au-Ag/B-TiO<sub>2</sub>: photocatalytic HER reaction and photocatalytic CO<sub>2</sub>RR reaction. The sample Cd3Ti2 has the highest photocatalytic property, and the H<sub>2</sub> generation efficiency under the full solar spectrum is 15.97 mmol·h<sup>-1</sup>·g<sup>-1</sup>. Its good stability is demonstrated by maintaining 81.3% of performance after 24 h cycles of reactions. The CO<sub>2</sub>RR was performed with the CH<sub>4</sub> yield of 14.2 μmol·h<sup>-1</sup>·g<sup>-1</sup> and the CO yield of 113.9 μmol·h<sup>-1</sup>·g<sup>-1</sup>. High-performance benefits from coordinating the action mechanism between the electric field at the interface and the plasma electromagnetic field coupling. It helps to reduce the random migration of low-energy photo-generated electrons and holes, which improves the directional charge transfer kinetics. The FDTD simulations and DFT calculations help to establish the photocatalytic enhancement mechanism. This work is of great significance for understanding the structure-property-catalysis interplays of plasmonic metal-based heterostructures and realizing the rational design of plasmon-enhanced catalysis systems.

### CRediT authorship contribution statement

Shengchao Yang and Zhiyong Liu proposed and conceptualized this project. Qi Li and Ruihan Liu designed the experiments. Qi Li carried out the experiments and characterizations. Yufan Huang, Yuwei Liang, and Chunling Hu participated in the experiments or characterizations. Qi Li and Yufan Huang analyzed the results and drew the figures. Qi Li wrote the original draft. Zhiyong Liu, Jichang Liu, Yanlong Tai, and Yongsheng Li reviewed and edited the manuscript. Zhiyong Liu and Shengchao Yang funded this research. Zhiyong Liu, Shengchao Yang, and Yongsheng Li provided the necessary conditions for this research and participated in discussions during data analysis.

### Declaration of Competing Interest

The authors declare that they have no known competing financial interests or personal relationships that could have appeared to influence the work reported in this paper.

### Data availability

No data was used for the research described in the article.

### Acknowledgements

This work was financially supported by the National Key Research and Development Program of China (2022YFF1202500, 2022YFF1202502), the National Natural Science Foundation of China (62071459), Subject Arrangement Foundation of Shenzhen (JCYJ20180507182057026), and International Science and Technology Cooperation Project of Bingtuan (No. 2022BC008). In particular, Shengchao Yang would like to thank Prof. Enrico Benassi for fruitful discussions and suggestions. The authors would like to express their gratitude to EditSprings (<https://www.editsprings.cn>) for the expert linguistic services provided.

### Appendix A. Supporting information

Supplementary data associated with this article can be found in the online version at [doi:10.1016/j.apcatb.2023.122700](https://doi.org/10.1016/j.apcatb.2023.122700).

### References

- [1] H. Kumagai, Y. Tamaki, O. Ishitani, Photocatalytic systems for CO<sub>2</sub> reduction: metal-complex photocatalysts and their hybrids with photofunctional solid

- materials, *Acc. Chem. Res.* 55 (2022) 978–990, <https://doi.org/10.1021/acs.accounts.1c00705>.
- [2] P. Zhang, H. Liu, X. Li, Photo-reduction synthesis of Cu nanoparticles as plasmon-driven non-semiconductor photocatalyst for overall water splitting, *Appl. Surf. Sci.* 535 (2021), 147720, <https://doi.org/10.1016/j.apsusc.2020.147720>.
- [3] L. Yuan, Z. Geng, B. Fan, F. Guo, C. Han, State-of-the-art progress in tracking plasmon-mediated photoredox catalysis, *Pure Appl. Chem.* 93 (2021) 509–524, <https://doi.org/10.1515/pac-2021-0205>.
- [4] G.-Y. Yao, Z.-Y. Zhao, Q.-L. Liu, X.-D. Dong, Q.-M. Zhao, Theoretical calculations for localized surface plasmon resonance effects of Cu/TiO<sub>2</sub> nanosphere: Generation, modulation, and application in photocatalysis, *Sol. Energy Mater. Sol. Cells* 208 (2020), 110385, <https://doi.org/10.1016/j.solmat.2019.110385>.
- [5] D. Gao, J. Xu, L. Wang, B. Zhu, H. Yu, J. Yu, Optimizing atomic hydrogen desorption of sulfur-rich NiS<sub>1+x</sub> cocatalyst for boosting photocatalytic H<sub>2</sub> evolution, *Adv. Mater.* 34 (2022), 2108475, <https://doi.org/10.1002/adma.202108475>.
- [6] M. Humayun, H. Ullah, Z.-E. Cheng, A.A. Tahir, W. Luo, C. Wang, Au surface plasmon resonance promoted charge transfer in Z-scheme system enables exceptional photocatalytic hydrogen evolution, *Appl. Catal. B* 310 (2022), 121322, <https://doi.org/10.1016/j.apcatb.2022.121322>.
- [7] W. Zhong, J. Xu, P. Wang, B. Zhu, J. Fan, H. Yu, Novel core-shell Ag@AgSe<sub>x</sub> nanoparticle co-catalyst: In situ surface selenization for efficient photocatalytic H<sub>2</sub> production of TiO<sub>2</sub>, *Chin. J. Catal.* 43 (2022) 1074–1083, [https://doi.org/10.1016/s1872-2067\(21\)63969-4](https://doi.org/10.1016/s1872-2067(21)63969-4).
- [8] D. Liu, C. Xue, Plasmonic coupling architectures for enhanced photocatalysis, *Adv. Mater.* 33 (2021), 2005738, <https://doi.org/10.1002/adma.202005738>.
- [9] F.V.A. Camargo, Y. Ben-Shahar, T. Nagahara, Y.E. Panfil, M. Russo, U. Banin, G. Cerullo, Visualizing ultrafast electron transfer processes in semiconductor-metal hybrid nanoparticles: toward excitonic-plasmonic light harvesting, *Nano Lett.* 21 (2021) 1461–1468, <https://doi.org/10.1021/acs.nanolett.0c04614>.
- [10] K. Chen, S.-J. Ding, Z.-J. Luo, G.-M. Pan, J.-H. Wang, J. Liu, L. Zhou, Q.-Q. Wang, Largely enhanced photocatalytic activity of Au/XS<sub>2</sub>/Au (X = Re, Mo) antenna-reactor hybrids: charge and energy transfer, *Nanoscale* 10 (2018) 4130–4137, <https://doi.org/10.1039/c7nr09362d>.
- [11] Y. Li, M. Wen, Y. Wang, G. Tian, C. Wang, J. Zhao, Plasmonic hot electrons from oxygen vacancies for infrared light-driven catalytic CO<sub>2</sub> reduction on Bi<sub>2</sub>O<sub>3-x</sub>, *Angew. Chem. Int. Ed.* 60 (2021) 910–916, <https://doi.org/10.1002/anie.202010156>.
- [12] M. Dhiman, A. Maity, A. Das, R. Belgamwar, B. Chalke, Y. Lee, K. Sim, J.-M. Nam, V. Polshettiwar, Plasmonic colloidosomes of black gold for solar energy harvesting and hotspots directed catalysis for CO<sub>2</sub> to fuel conversion, *Chem. Sci.* 10 (2019) 6594–6603, <https://doi.org/10.1039/c9sc02369k>.
- [13] R. Li, W.-H. Cheng, M.H. Richter, J.S. DuChene, W. Tian, C. Li, H.A. Atwater, Unassisted highly selective gas-phase CO<sub>2</sub> reduction with a plasmonic Au/p-GaN photocatalyst using H<sub>2</sub>O as an electron donor, *ACS Energy Lett.* 6 (2021) 1849–1856, <https://doi.org/10.1021/acsenenergylett.1c00392>.
- [14] M. Sistani, M.G. Bartmann, N.A. Gusken, R.F. Oulton, H. Keshmiri, L. Minh Anh, Z. S. Momtaz, M.I. Den Hertog, A. Lugstein, Plasmon-driven hot electron transfer at atomically sharp metal-semiconductor nanojunctions, *ACS Photonics* 7 (2020) 1642–1648, <https://doi.org/10.1021/acsp Photonics.0c00557>.
- [15] I. Kherbouche, Y. Luo, N. Felidj, C. Mangeney, Plasmon-mediated surface functionalization: new horizons for the control of surface chemistry on the nanoscale, *Chem. Mater.* 32 (2020) 5442–5454, <https://doi.org/10.1021/acs.chemmater.0c00921>.
- [16] W. Hou, S.B. Cronin, A review of surface plasmon resonance-enhanced photocatalysis, *Adv. Funct. Mater.* 23 (2013) 1612–1619, <https://doi.org/10.1002/adfm.201202148>.
- [17] L. Ma, Y.-L. Chen, D.-J. Yang, H.-X. Li, S.-J. Ding, L. Xiong, P.-L. Qin, X.-B. Chen, Multi-interfacial plasmon coupling in multigap (Au/AgAu)/CdS core-shell hybrids for efficient photocatalytic hydrogen generation, *Nanoscale* 12 (2020) 4383–4392, <https://doi.org/10.1039/c9nr09696e>.
- [18] J.-L. Yang, Y.-L. He, H. Ren, H.-L. Zhong, J.-S. Lin, W.-M. Yang, M.-D. Li, Z.-L. Yang, H. Zhang, Z.-Q. Tian, J.-F. Li, Boosting photocatalytic hydrogen evolution reaction using dual plasmonic antennas, *ACS Catal.* 11 (2021) 5047–5053, <https://doi.org/10.1021/acscatal.1c00795>.
- [19] P.-F. Wang, K. Chen, S. Ma, W. Wang, Y.-H. Qiu, S.-J. Ding, S. Liang, Q.-Q. Wang, Asymmetric synthesis of Au-CdSe core-shell nanorods for plasmon-enhanced visible-light-driven hydrogen evolution, *Nanoscale* 12 (2020) 687–694, <https://doi.org/10.1039/c9nr09370b>.
- [20] X. Wang, R. Long, D. Liu, D. Yang, C. Wang, Y. Xiong, Enhanced full-spectrum water splitting by confining plasmonic Au nanoparticles in N-doped TiO<sub>2</sub> bowl nanoarrays, *Nano Energy* 24 (2016) 87–93, <https://doi.org/10.1016/j.nanoen.2016.04.013>.
- [21] Y. Gao, W. Nie, Q. Zhu, X. Wang, S. Wang, F. Fan, C. Li, The polarization effect in surface-plasmon-induced photocatalysis on Au/TiO<sub>2</sub> nanoparticles, *Angew. Chem. Int. Ed.* 59 (2020) 18218–18223, <https://doi.org/10.1002/anie.202007706>.
- [22] E. Vahidzadeh, S. Zeng, A.P. Manuel, S. Riddell, P. Kumar, K.M. Alam, K. Shankar, Asymmetric Multipole Plasmon-Mediated Catalysis Shifts the Product Selectivity of CO<sub>2</sub> Photoreduction toward C<sub>2+</sub> Products, *ACS Appl. Mater. Interfaces* 13 (2021) 7248–7258, <https://doi.org/10.1021/acsaami.0c21067>.
- [23] T. Shao, X. Wang, H. Dong, S. Liu, D. Duan, Y. Li, P. Song, H. Jiang, Z. Hou, C. Gao, Y. Xiong, A stacked plasmonic metamaterial with strong localized electric field enables highly efficient broadband light-driven CO<sub>2</sub> hydrogenation, *Adv. Mater.* 34 (2022), 2202367, <https://doi.org/10.1002/adma.202202367>.
- [24] F.S. Lim, S.T. Tan, Y. Zhu, J.-W. Chen, B. Wu, H. Yu, J.-M. Kim, R.T. Ginting, K. S. Lau, C.H. Chia, H. Wu, M. Gu, W.S. Chang, Tunable Plasmon-Induced Charge

- Transport and Photon Absorption of Bimetallic Au-Ag Nanoparticles on ZnO Photoanode for Photoelectrochemical Enhancement under Visible Light, *J. Phys. Chem. C* 124 (2020) 14105–14117, <https://doi.org/10.1021/acs.jpcc.0c03967>.
- [25] S. Linic, P. Christopher, D.B. Ingram, Plasmonic-metal nanostructures for efficient conversion of solar to chemical energy, *Nat. Mater.* 10 (2011) 911–921, <https://doi.org/10.1038/nmat3151>.
- [26] X. Yue, J. Hou, H. Zhao, P. Wu, Y. Guo, Q. Shi, L. Chen, S. Peng, Z. Liu, G. Cao, Au-Ag alloy nanoparticles with tunable cavity for plasmon-enhanced photocatalytic H<sub>2</sub> evolution, *J. Energy Chem.* 49 (2020) 1–7, <https://doi.org/10.1016/j.jechem.2020.01.005>.
- [27] X. Yue, J. Hou, Y. Zhang, P. Wu, Y. Guo, S. Peng, Z. Liu, H. Jiang, Improved CdS photocatalytic H<sub>2</sub> evolution using Au-Ag nanoparticles with tunable plasmon-enhanced resonance energy transfer, *Dalton Trans.* 49 (2020) 7467–7473, <https://doi.org/10.1039/d0dt01110j>.
- [28] X. An, D. Stelter, T. Keyes, B.M. Reinhard, Plasmonic Photocatalysis of Urea Oxidation and Visible-Light Fuel Cells, *Chem* 5 (2019) 2228–2242, <https://doi.org/10.1016/j.chempr.2019.06.014>.
- [29] X. An, J.C. Kays, I.V. Lightcap, T. Ouyang, A.M. Dennis, B.M. Reinhard, Wavelength-dependent bifunctional plasmonic photocatalysis in Au/chalcopyrite hybrid nanostructures, *ACS Nano* 16 (2022) 6813–6824, <https://doi.org/10.1021/acsnano.2c01706>.
- [30] J. Wang, Y. Shi, Y. Wang, Z. Li, Rational Design of Metal Halide Perovskite Nanocrystals for Photocatalytic CO<sub>2</sub> Reduction: Recent Advances, Challenges, and Prospects, *ACS Energy Lett.* 7 (2022) 2043–2059, <https://doi.org/10.1021/acsenrgylett.2c00752>.
- [31] Q. Li, P. Wu, Y. Huang, P. Chen, K. Wu, J. Wu, Y. Luo, L. Wang, S. Yang, Z. Liu, X. Guo, A novel lattice-embedded ZnO@TiO<sub>2</sub>(B) nanoflowers promotes photocatalytic production of H<sub>2</sub>, *Int. J. Hydrog. Energy* 47 (2022) 15641–15654, <https://doi.org/10.1016/j.ijhydene.2022.03.0910360-3199>.
- [32] G. Kresse, J. Furthmüller, Efficient iterative schemes for ab initio total-energy calculations using a plane-wave basis set, *Phys. Rev. B* 54 (1996) 11169–11186, <https://doi.org/10.1103/PhysRevB.54.11169>.
- [33] Perdew, Chevary, Vosko, Jackson, Pederson, Singh, Fiolhais, Atoms, molecules, solids, and surfaces: Applications of the generalized gradient approximation for exchange and correlation, *Phys. Rev. B* 46 (1992) 6671–6687, <https://doi.org/10.1103/PhysRevB.46.6671>.
- [34] L. Qiao, G. Duan, S. Zhang, Y. Ren, Y. Sun, Y. Tang, P. Wan, R. Pang, Y. Chen, A. G. Russell, M. Fan, Electrochemical ammonia synthesis catalyzed with a CoFe layered double hydroxide - A new initiative in clean fuel synthesis, *J. Clean. Prod.* 250 (2020), 119525, <https://doi.org/10.1016/j.jclepro.2019.119525>.
- [35] J. Klimes, D.R. Bowler, A. Michaelides, Van der Waals density functionals applied to solids, *Phys. Rev. B* 83 (2011), 195131, <https://doi.org/10.1103/PhysRevB.83.195131>.
- [36] N.-Y. Huang, H. He, S. Liu, H.-L. Zhu, Y.-J. Li, J. Xu, J.-R. Huang, X. Wang, P.-Q. Liao, X.-M. Chen, Electrostatic Attraction-Driven Assembly of a Metal-Organic Framework with a Photosensitizer Boosts Photocatalytic CO<sub>2</sub> Reduction to CO, *J. Am. Chem. Soc.* 143 (2021) 17424–17430, <https://doi.org/10.1021/jacs.1c05839>.
- [37] L. He, W. Zhang, S. Liu, Y. Zhao, Three-dimensional porous N-doped graphitic carbon framework with embedded CoO for photocatalytic CO<sub>2</sub> reduction, *Appl. Catal. B* 298 (2021), 120546, <https://doi.org/10.1016/j.apcatb.2021.120546>.
- [38] Q. Bi, K. Hu, J. Chen, Y. Zhang, M.S. Riaz, J. Xu, Y. Han, F. Huang, Black phosphorus coupled black titania nanocomposites with enhanced sunlight absorption properties for efficient photocatalytic CO<sub>2</sub> reduction, *Appl. Catal. B* 295 (2021), 120211, <https://doi.org/10.1016/j.apcatb.2021.120211>.
- [39] S. Liu, X. Guo, W. Wang, Y. Yang, C. Zhu, C. Li, W. Lin, Q. Tian, Y. Liu, CdS-Cu<sub>1.81</sub>S heteronanorods with continuous sublayer for photocatalytic hydrogen production, *Appl. Catal. B* 303 (2022), 120909, <https://doi.org/10.1016/j.apcatb.2021.120909>.
- [40] L. Huang, D. Bao, J. Li, X. Jiang, X. Sun, Construction of Au modified direct Z-scheme g-C<sub>3</sub>N<sub>4</sub>/defective ZnO heterostructure with stable high-performance for tetracycline degradation, *Appl. Surf. Sci.* 555 (2021), 149696, <https://doi.org/10.1016/j.apsusc.2021.149696>.
- [41] M.K. Kumar, G. Naresh, V.V. Kumar, B.S. Vasista, B. Sasikumar, A. Venugopal, Improved H<sub>2</sub> yields over Cu-Ni-TiO<sub>2</sub> under solar light irradiation: Behaviour of alloy nano particles on photocatalytic H<sub>2</sub>O splitting, *Appl. Catal. B* 299 (2021), 120654, <https://doi.org/10.1016/j.apcatb.2021.120654>.
- [42] X. Liu, X. Shen, B. Sa, Y. Zhang, X. Li, H. Xue, Piezotronic-enhanced photocatalytic performance of heterostructured BaTiO<sub>3</sub>/SrTiO<sub>3</sub> nanofibers, *Nano Energy* 89 (2021), 106391, <https://doi.org/10.1016/j.nanoen.2021.106391>.
- [43] L. Chen, X. Liang, H. Wang, Q. Xiao, X. Qiu, Ultra-thin carbon nitride nanosheets for efficient photocatalytic hydrogen evolution, *Chem. Eng. J.* 442 (2022), 136115, <https://doi.org/10.1016/j.cej.2022.136115>.
- [44] A. Sabbah, I. Shown, M. Qorbani, F.-Y. Fu, T.-Y. Lin, H.-L. Wu, P.-W. Chung, C.-I. Wu, S.R.M. Santiago, J.-L. Shen, K.-H. Chen, L.-C. Chen, Boosting photocatalytic CO<sub>2</sub> reduction in a ZnS/ZnIn<sub>2</sub>S<sub>4</sub> heterostructure through strain-induced direct Z-scheme and a mechanistic study of molecular CO<sub>2</sub> interaction thereon, *Nano Energy* 93 (2022), 106809, <https://doi.org/10.1016/j.nanoen.2021.106809>.
- [45] C. Lai, F. Xu, M. Zhang, B. Li, S. Liu, H. Yi, L. Li, L. Qin, X. Liu, Y. Fu, N. An, H. Yang, X. Huo, X. Yang, H. Yan, Facile synthesis of CeO<sub>2</sub>/carbonate doped Bi<sub>2</sub>O<sub>3</sub>/CO<sub>2</sub> Z-scheme heterojunction for improved visible-light photocatalytic performance: Photodegradation of tetracycline and photocatalytic mechanism, *J. Colloid Interface Sci.* 588 (2021) 283–294, <https://doi.org/10.1016/j.jcis.2020.12.073>.
- [46] W. Yang, S. Tang, Z. Wei, X. Chen, C. Ma, J. Duan, R. Tan, Separate-free BiPO<sub>4</sub>/graphene aerogel with 3D network structure for efficient photocatalytic mineralization by adsorption enrichment and photocatalytic degradation, *Chem. Eng. J.* 421 (2021), 129720, <https://doi.org/10.1016/j.cej.2021.129720>.
- [47] H. Huang, R. Shi, Z. Li, J. Zhao, C. Su, T. Zhang, Triphase Photocatalytic CO<sub>2</sub> Reduction over Silver-Decorated Titanium Oxide at a Gas-Water Boundary, *Angew. Chem. Int. Ed.* 61 (2022), e202200802, <https://doi.org/10.1002/anie.202200802>.
- [48] Z. Tang, W. He, Y. Wang, Y. Wei, X. Yu, J. Xiong, X. Wang, X. Zhang, Z. Zhao, J. Liu, Ternary heterojunction in rGO-coated Ag/Cu<sub>2</sub>O catalysts for boosting selective photocatalytic CO<sub>2</sub> reduction into CH<sub>4</sub>, *Appl. Catal. B* 311 (2022), 121371, <https://doi.org/10.1016/j.apcatb.2022.121371>.
- [49] Q. Zhu, Y. Xuan, K. Zhang, K. Chang, Enhancing photocatalytic CO<sub>2</sub> reduction performance of g-C<sub>3</sub>N<sub>4</sub>-based catalysts with non-noble plasmonic nanoparticles, *Appl. Catal. B* 297 (2021), 120440, <https://doi.org/10.1016/j.apcatb.2021.120440>.
- [50] P. Minh-Thuan, A. Hussain, B. Dai-Phat, N. Truc-Mai Thi, S.-J. You, Y.-F. Wang, Surface plasmon resonance enhanced photocatalysis of Ag nanoparticles-decorated Bi<sub>2</sub>S<sub>3</sub> nanorods for NO degradation, *Environ. Technol. Innov.* 23 (2021), 101755, <https://doi.org/10.1016/j.eti.2021.101755>.
- [51] J. Li, S.K. Cushing, F. Meng, T.R. Senty, A.D. Bristow, N. Wu, Plasmon-induced resonance energy transfer for solar energy conversion, *Nat. Photon.* 9 (2015) 601–607, <https://doi.org/10.1038/nphoton.2015.142>.
- [52] J. Li, S.K. Cushing, P. Zheng, F. Meng, D. Chu, N. Wu, Plasmon-induced photonic and energy-transfer enhancement of solar water splitting by a hematite nanorod array, *Nat. Commun.* 4 (2013) 2651, <https://doi.org/10.1038/ncomms3651>.
- [53] Z. Xie, W. Xu, F. Fang, K. Zhang, X. Yu, K. Chang, Gel-assisted synthesis of CZTS for visible-light photocatalytic reduction reaction, *Chem. Eng. J.* 429 (2022), 132364, <https://doi.org/10.1016/j.cej.2021.132364>.
- [54] B. Wang, C. Yan, G. Xu, X. Shu, J. Lv, Y. Wu, Highly efficient solar-driven photocatalytic hydrogen evolution with FeMoS<sub>4</sub>/mpg-C<sub>3</sub>N<sub>4</sub> heterostructure, *Chem. Eng. J.* 427 (2022), 131507, <https://doi.org/10.1016/j.cej.2021.131507>.
- [55] L. Wang, J. Guan, H. Han, M. Yao, J. Kang, M. Peng, D. Wang, J. Xu, J. Hao, Enhanced photocatalytic removal of ozone by a new chlorine-radical-mediated strategy, *Appl. Catal. B* 306 (2022), 121130, <https://doi.org/10.1016/j.apcatb.2022.121130>.
- [56] H. Gao, P. Zhang, J. Zhao, Y. Zhang, J. Hu, G. Shao, Plasmon enhancement on photocatalytic hydrogen production over the Z-scheme photosynthetic heterojunction system, *Appl. Catal. B* 210 (2017) 297–305, <https://doi.org/10.1016/j.apcatb.2017.03.050>.
- [57] S. Kamimura, S. Yamashita, S. Abe, T. Tsubota, T. Ohno, Effect of core@shell (Au@Ag) nanostructure on surface plasmon-induced photocatalytic activity under visible light irradiation, *Appl. Catal. B* 211 (2017) 11–17, <https://doi.org/10.1016/j.apcatb.2017.04.028>.
- [58] N. Li, X. Chen, J. Wang, X. Liang, L. Ma, X. Jing, D.-L. Chen, Z. Li, ZnSe Nanorods-CsSnCl<sub>3</sub> Perovskite Heterojunction Composite for Photocatalytic CO<sub>2</sub> Reduction, *ACS Nano* 16 (2022) 3332–3340, <https://doi.org/10.1021/acsnano.1c11442>.
- [59] P. Xia, X. Pan, S. Jiang, J. Yu, B. He, P.M. Ismail, W. Bai, J. Yang, L. Yang, H. Zhang, M. Cheng, H. Li, Q. Zhang, C. Xiao, Y. Xie, Designing a Redox Heterojunction for Photocatalytic "Overall Nitrogen Fixation" under Mild Conditions, *Adv. Mater.* 34 (2022), 2200563, <https://doi.org/10.1002/adma.202200563>.
- [60] S. Xie, Y. Li, B. Sheng, W. Zhang, W. Wang, C. Chen, J. Li, H. Sheng, J. Zhao, Self-reconstruction of paddle-wheel copper-node to facilitate the photocatalytic CO<sub>2</sub> reduction to ethane, *Appl. Catal. B* 310 (2022), 121320, <https://doi.org/10.1016/j.apcatb.2022.121320>.
- [61] F. Wang, R. Fang, X. Zhao, X.-P. Kong, T. Hou, K. Shen, Y. Li, Ultrathin nanosheet assembled multishelled superstructures for photocatalytic CO<sub>2</sub> reduction, *ACS Nano* 16 (2022) 4517–4527, <https://doi.org/10.1021/acsnano.1c10958>.
- [62] L. Hurtado, A. Mohan, U. Ulmer, R. Natividad, A.A. Tountas, W. Sun, L. Wang, B. Kim, M.M. Sain, G.A. Ozin, Solar CO<sub>2</sub> hydrogenation by photocatalytic foams, *Chem. Eng. J.* 435 (2022), 134864, <https://doi.org/10.1016/j.cej.2022.134864>.
- [63] O. Dumele, L. Dordevic, H. Sai, T.J. Cotey, M.H. Sangji, K. Sato, A.J. Dannenhoffer, S.I. Stupp, Photocatalytic Aqueous CO<sub>2</sub> Reduction to CO and CH<sub>4</sub> Sensitized by Ullazine Supramolecular Polymers, *J. Am. Chem. Soc.* 144 (2022) 3127–3136, <https://doi.org/10.1021/jacs.1c12155>.
- [64] J. Zhao, M. Ji, H. Chen, Y.-X. Weng, J. Zhong, Y. Li, S. Wang, Z. Chen, J. Xia, H. Li, Interfacial chemical bond modulated Bi<sub>10</sub>S<sub>27</sub>Br<sub>3</sub>/g-C<sub>3</sub>N<sub>4</sub> Z-scheme heterojunction for enhanced photocatalytic CO<sub>2</sub> conversion, *Appl. Catal. B* 307 (2022), 121162, <https://doi.org/10.1016/j.apcatb.2022.121162>.
- [65] G. Yu, J. Qian, P. Zhang, B. Zhang, W. Zhang, W. Yan, G. Liu, Collective excitation of plasmon-coupled Au-nanochain boosts photocatalytic hydrogen evolution of semiconductor, *Nat. Commun.* 10 (2019) 4912, <https://doi.org/10.1038/s41467-019-12853-8>.
- [66] J. Hao, H. He, S. Gong, J. Fan, Q. Xu, Y. Min, WN coupled with Bi nanoparticles to enhance the localized surface plasmon resonance effect for photocatalytic hydrogen evolution, *ACS Appl. Mater. Interfaces* 13 (2021) 19884–19893, <https://doi.org/10.1021/acsami.0c22815>.
- [67] M. Kou, W. Liu, Y. Wang, J. Huang, Y. Chen, Y. Zhou, Y. Chen, M. Ma, K. Lei, H. Xie, P.K. Wong, L. Ye, Photocatalytic CO<sub>2</sub> conversion over single-atom MoN<sub>2</sub> sites of covalent organic framework, *Appl. Catal. B* 291 (2021), 120146, <https://doi.org/10.1016/j.apcatb.2021.120146>.